Sede Amministrativa: Università degli Studi di Padova

Dipartimento di Fisica e Astronomia Galileo Galilei

Corso di Dottorato di Ricerca in **Physics**
Ciclo **XXXV**

Van der Waals effects with Density Functional Theory: exact approach for small isolated systems and improved description of interlayer bonding in TiS2.

Tesi redatta con il contributo finanziario della Fondazione Cariparo.

Coordinatore: Ch.mo Prof. Giulio Monaco
Supervisore: Ch.mo Dott. PierLuigi Silvestrelli
Co-Supervisore: Ch.mo Dott. Alberto Ambrosetti

Dottorando: Matteo Ricci

Contents

1 Introduction

Identified in 1873 [1], the van der Waals (vdW) interaction, is a force that today attracts more interest than ever. It was first introduced in his doctoral thesis by Johannes Diderik van der Waals at Leiden University. The existence of the vdW force is today well established. It is present everywhere, but its variation from one environment to another and its complex manifestations still pose challenging questions nearly one hundred years after van der Waals was awarded the Nobel Prize in physics. In physical-chemistry terminology, the possible sources of the vdW interaction are considered to be the following

- Two permanent dipoles (Keesom force)
- A permanent dipole and a corresponding induced dipole (Debye force)
- Two instantaneously induced dipoles (London dispersion forces)

In the condensed-matter community, typically just the last situation mentioned, which is a pure quantum phenomenon, is considered the real source of vdW interactions.

From a computational point of view Density Functional Theory (DFT) represents one of the most well-established approach nowadays applied to study the structural and electronic properties of condensed matter from first principles, mainly, because of its high accuracy, which comes at a reasonable computational cost. Although current, approximated density functionals allow a quantitative description at much lower computational cost than other first principles methods, they fail [2] to properly include vdW interactions. These originate from correlated charge oscillations in separate fragments of matter, and the leading component (namely, the lowest-order perturbative contribution) is represented by the R^{-6} vdW interaction [3] due to correlated instantaneous dipole fluctuations. A proper description of these interactions is very important because they play a fundamental role in determining the structure, stability, and function of a wide variety of systems, including molecules, clusters, proteins, nanostructured materials, and molecular solids and liquids, and in adsorption processes of fragments weakly interacting with a substrate (“physisorbed”).

Overall, there are now several kinds of schemes to include vdW interaction in DFT calculations. Among them, it is worth to mention the earliest approaches, in which atom-based pair potentials were computed and coupled with an empirical damped dispersion correction (see for example ref. [4]). More recently newer and more efficient methods, such as the those based on the use of Wannier functions[5, 6, 7, 8, 9] or the Many Body Dispersion (MBD) model[10] were developed. Notable success has been achieved by non-local exchange-correlation density functionals as well, for which the ground state energy of a system is computed by means of a spatial integration over a non-local correlation kernel, in which usually there is a dependency on one or more empirical fitting parameters. Among these latter density functionals schemes, it is worth to mention those proposed by Vydrov and Van Voorhis[11] [12] (see Appendix).

In this Thesis we propose to improve the description of vdW effects with DFT considering two approaches. In the first [13] one we derive a novel sum-rule approach, applied to simple, but emblematic, systems such as the Hydrogen atom, a system of quantum harmonic oscillators and a particle confined in a spherical well potential. In this context, firstly, we derive exact expressions concerning both polarizability and vdW density functionals, giving anlytical results when it is possible and then we make a comparison between our results and those obtained within popular, well established theoretical vdW approaches.

In the second part [14] of the Thesis instead we mainly focus on a the description of vdW interactions with DFT considering the specific class of layered materials, analyzing one of them, TiS_2, in detail. We characterize the way vdW interactions are modeled by state of the art Density Functional Theory (DFT) methods, particularly focusing on the electron density distribution, being this latter the physical quantity lying at the core of DFT. We provide extensive benchmarking for the electron density distribution, first by reproducing reported hortcomings of standard approaches, and, then, on the basis of physical considerations, by generating a novel pseudopotential whose integration in a DFT scheme almost totally overcome the issues mentioned above.

2 Polarizability and van der Waals Density Functionals: exact results for small systems

In this section we adopt a novel sum-rule approach developing an exact theoretical framework for polarizability and asymptotic van der Waals correlation energy functionals of small isolated objects [13]. This is done by extending the completeness sum-rule approach of Dalgarno and Lewis[15]. The adopted sum-rule approach implies general validity of our theory, enabling exact benchmarking of van der Waals density functionals, and direct inspection of the subtle long-range correlation effects that constitute a major challenge for (semi-)local approximations. Our method will also enable direct comparison with the popular Vydrov-van Voorhis density functional. The derived functionals require only monomer groundstate properties as input which means that functional evaluation proceeds via solution of a single position-space differential equation, without the usual summations over excited states or frequency integrations. Explicit functional forms are reported for reference physical systems, including atomic hydrogen and single electrons subject to harmonic confinement, and immersed in a spherical-well potential.

2.1 Polarizability functional

The response of a system to a static electric field is one of the most interesting microscopic phenomena in condensed matter physics. In particular, the linear response of a system to an external perturbation leads to the concept of polarizability. In order to introduce the physical concept, let us consider a very well know case: an hydrogen atom (with fixed nucleus) under the effect of a weak, static electric field $\mathcal{E}$ along the z axis. For this physical system, the Hamiltonian reads

$$H(\mathcal{E}) = \frac{p^2}{2\,m} - \frac{e^2}{r} - |e|\,\mathcal{E}\,z \tag{1}$$

where the single electron is described by the mass m, the charge $-|e|$ and the coordinate r, centered on the atomic nucleus. In this scenario, the polarizability is a quantity whose purpose is to describe how much the weak electric field deforms the electron cloud with respect to the unperturbed case. An expression for α, valid not only for the use case presented, can be obtained through the application of non-degenerate perturbation theory and allows us to express the static polarizability for the $|m\rangle$ state in terms of the following summation

$$\alpha_m = 2 \sum_{m \neq n} \frac{\langle m|\, D_z \,|n\rangle \, \langle n|\, D_z \,|m\rangle}{E_n - E_m} \tag{2}$$

where E_m is the eigenvalue of the unperturbed m state and $D_z = -|e|z$ is the induced electric dipole moment. Note that for parity $\langle m|\, D_z \,|m\rangle = 0$ for any eigenstate $|m\rangle$, hence the summation runs only over those states $\neq n$. Here, one must include both bound states and the continuous part of the spectrum, which contributes for approximately one third of the final value of α [63]. An elegant solution of Eq.(2), which does not require the explicit summation to be carried out, has been proposed by Dalgarno and Lewis in 1955 [15].

Le us now assume $m = 0$ (groundstate polarizability). In order to evaluate (2), we seek an operator $\hat{F}$ such that, for all $m \neq 0$,

$$\langle n|\hat{F}|0\rangle = -\frac{\langle n|\hat{D}_z|0\rangle}{E_n - E_0}\,, \tag{3}$$

Then (2) becomes

$$\alpha_0 = -2\sum_{n\neq 0}\langle 0|\hat{D}_z|n\rangle\langle n|\hat{F}|0\rangle = -2\sum_{all\,n}\langle 0|\hat{D}_z|n\rangle\langle n|\hat{F}|0\rangle + 2\langle 0|\hat{D}_z|0\rangle\langle 0|\hat{F}|0\rangle\,. \tag{4}$$

Using a sum rule (completeness relation) $\sum_{all\,n}|n\rangle\langle n| = 1$ and noting $\langle 0|\hat{D}_z|0\rangle = 0$ for an isotropic system, we reduce the last equation to

$$\alpha_0 = -2\langle 0|\hat{D}_z\hat{F}|0\rangle\,. \tag{5}$$

The operator $\hat{F}$ satisfies a commutator relationship derived as follows. Multiply (3) through by the energy denominator, obtaining

$$(E_n - E_0)\langle n|\hat{F}|0\rangle = -\langle n|\hat{D}_z|0\rangle\,, \tag{6}$$

and since $E_n\langle n| = \langle n|\hat{H}$ and $E_0|0\rangle = \hat{H}|0\rangle$, (6) $\langle n|[\hat{H},\hat{F}]|0\rangle = -\langle n|\hat{D}_z|0\rangle$. To satisfy this relation it is sufficient that

$$[\hat{H},\hat{F}]|0\rangle = -\hat{D}_z|0\rangle\,. \tag{7}$$

If $\hat{F}$ is a particular solution of (7), then $\hat{F} + \hat{G}$ is another solution, where $\hat{G}$ is any operator such that $\hat{G}|0\rangle = 0$. Since $\langle n|0\rangle = 0$ for $n \neq 0$, a general solution can be expressed as

$$G = \sum_{m,n:n\neq 0} g_{mn}|m\rangle\langle n| \tag{8}$$

where g_{mn} is arbitrary. The existence of this very broad range of solutions allows us to seek a solution that is a *multiplicative, local* operator such that $(\hat{F}\psi)(\mathbf{X}) = F(\mathbf{X})\psi(\mathbf{X})$. Here $\mathbf{X} = (\mathbf{r}_1, \mathbf{r}_2, ..., \mathbf{r}_N)$ is the many-electron position variable and ψ is a many-electron wavefunction. Since $\hat{H}$ is a differential operator in position space, the commutation relation (7) then becomes a single position-space differential equation for the unknown function $F(\mathbf{X})$, with input from the groundstate wavefunction $\psi_0(\mathbf{X}) \equiv \langle\mathbf{X}|0\rangle$. Once $F(\mathbf{X})$ is found, the static polarizability is evaluated via a spatial integration of the matrix element specified in Eq.(5). The differential equation (7) for $F(\mathbf{X})$ has solutions, and we exhibit these explicitly for three different one-electron cases below. The existence of such solutions verifies a posteriori that a local operator can solve (7). The derived sum rule approach is the core of the novel theoretical method [13] presented in this section and will be described in detail to obtain the ground state polarizability of three systems of relevant physical interest: the hydrogen atom, and an electron confined in a quantum harmonic oscillator (QHO) and a spherical well (SW) potential.

2.1.1 Hydrogen Atom

For the hydrogen atom ($N = 1$), we have $\hat{D}_z = -|e|z$ so that from (7) we can write $[\hat{H}, \hat{F}]|0\rangle = z|0\rangle$, where we have used atomic units (where $e = 1$). Since F was chosen to be a local operator (this choice will be justified a posteriori), the only non-vanishing terms in $[H, F]$ come from the commutation between kinetic energy and F. Hence

$$[H, F]|0\rangle = -\frac{1}{2}[\nabla^2, F]|0\rangle = -\frac{1}{2}\left[(\nabla^2 F)|0\rangle + 2(\vec{\nabla} F) \cdot (\vec{\nabla}|0\rangle)\right] . \tag{9}$$

Considering that $z = r\cos(\theta)$ is associated to the spherical harmonic $Y_0^1(\theta)$, we define $F(r, \theta) = f(r)\cos(\theta)$, and the Laplacian of F can be written as

$$-\nabla^2 F = -\frac{1}{r}\partial_r^2 F r + \frac{2F}{r^2} . \tag{10}$$

In the case of atomic H (where $V(r) = -1/r$), the gradient of the ground state wavefunction ψ_0 is $\vec{\nabla}\psi_0 = -\frac{\vec{r}}{r}\psi_0$, and considering that $z = r\cos(\theta)$, Eq. (7) can be finally recast as:

$$\partial_r^2 f - 2(1 - \frac{1}{r})\partial_r f - \frac{2}{r^2} f = -2r . \tag{11}$$

This equation admits the particular solution

$$f(r) = \left(\frac{r^2}{2} + r\right) . \tag{12}$$

Since Eq. (11) is a differential equation of second order, f is defined up to a combination of solutions of the associated homogeneous equation. Once we have an explicit expression for f, the exact static polarizability can be finally evaluated. Using $\psi_0(r) = (a_0\pi)^{-1/3}\exp(-\mathrm{r}/\mathrm{a}_0)$ as the Hydrogen atom ground state wave function, the evaluation of (5) leads to the well known result

$$\alpha_0 = \frac{9}{2}\, a_0^3 \tag{13}$$

where a_0 is the Bohr radius.

2.1.2 Quantum Harmonic Oscillator

The case of the charged quantum harmonic oscillator can be carried out within the exact same procedure applied for the hydrogen atom. We first define

$$|\tilde{\phi}\rangle = \sum_n \frac{|n\rangle\langle n|D_z|0\rangle}{E_0 - E_n} \, . \tag{14}$$

Then, carrying out some algebra, Eq. (7) can be recast as

$$(E_0 - H)|\tilde{\phi}\rangle = D_z\,|0\rangle \ , \tag{15}$$

an equation which will be useful later on as well. Considering a 3D harmonic oscillator of mass m, charge q and frequency ω_0 and assuming $\tilde{\phi}(r) = f(r)\cos(\theta)$ the above expression turns out to be

$$\left(\frac{3}{2}\,\omega_0 + \frac{\nabla^2}{2} - \frac{m\,\omega_0^2\,r^2}{2}\right) f(r)\cos(\theta)\,\psi_0 = -q\,z\,\psi_0 = -q\,r\cos(\theta)\,\psi_0 \tag{16}$$

where the ground state radial wave function reads

$$\psi_0(r) = \left(\frac{m\omega_0}{\pi}\right)^{3/4} e^{-m\,\omega_0\,r^2/2}$$

The radial component of Eq. (15) can be easily factorized (hereafter we assume $q = 1$ for notation simplicity)

$$\partial_r^2 f - 2(\omega_0 r - \frac{1}{r})\partial_r f - \frac{2}{r^2} f = -2r\,, \tag{17}$$

As in the hydrogen atom case, an analytical solution exists, namely:

$$f(r) = \frac{r}{\omega_0}\,. \tag{18}$$

Finally, by means of (5) we compute the ground state static polarizability for a charged quantum harmonic oscillator

$$\alpha_0 = \frac{1}{m\,\omega_0^2}\,. \tag{19}$$

2.1.3 Charged Particle in a Spherical Well Potential

The last system under consideration is a charged particle under the influence of a spherically-shaped potential. Assuming b to be the sphere radius and r the radial coordinate of the particle, the potential reads:

$$V(r) = \begin{cases} 0 & r < b \\ \infty & \text{otherwise} \end{cases}\,. \tag{20}$$

we are interested in the ground state static polarizability of the free particle confined within the sphere. Let us assume the particle to have charge $q = 1$, so Eq. (15) reads (we invert here the sign of $\tilde{\phi}$ with respect to the previous notation for convenience)

$$(E_0 - H)|\tilde{\phi}\rangle = z|0\rangle\,. \tag{21}$$

From the above equation it is thus evident that one can add to $|\tilde{\phi}\rangle$ any combination of those wavefunctions that are orthogonal to $z|0\rangle$: for instance, one can choose $|0\rangle$ itself, or any eigenstate with angular momentum other than $l = 1, l_z = 0$. Moreover, within the present procedure, one can factorize the Y_0^1 spherical harmonics (ie $\tilde{\phi}' \cos(\theta) = \tilde{\phi}$), obtaining the following radial equation

$$\frac{1}{2r}\partial_r^2 r\tilde{\phi}' - \frac{1}{r^2}\tilde{\phi}' + (E_0 - V(r))\tilde{\phi}' = r\psi_0\,. \tag{22}$$

One could then solve the above equation by noting that the independent solutions of the associated homogeneous equation are known:

$$j_1(r) = \frac{\cos(kr)}{kr} - \frac{\sin(kr)}{(kr)^2} \tag{23}$$

$$\eta_1(r) = \frac{\sin(kr)}{kr} + \frac{\cos(kr)}{(kr)^2} \tag{24}$$

where $k = \pi/b$. We note that these solutions do not satisfy the correct boundary conditions, since any eigenstate should vanish at $r = b$. A particular solution of Eq. (22) can be found as

$$\tilde{\phi}' = c_j j_1 + c_\eta \eta_1\,, \tag{25}$$

where

$$\partial_r c_j = -\eta_1 W^{-1} R \tag{26}$$

$$\partial_r c_\eta = j_1 W^{-1} R \tag{27}$$

Here $R = 2\,r\psi_0$ and W is the Wronskian: $W = j_1\partial_r\eta_1 - \eta_1\partial_r j_1$. After some algebra one finds that

$$\tilde{\phi}' = \sqrt{\frac{k^2}{2\,\pi^2}}\left(\frac{r}{2\,k^2}\cos(k\,r) + C_1 j_1 + C_2\eta_1\right)\,. \tag{28}$$

In order to keep $\tilde{\phi}'$ finite at $r = 0$ one has to set $C_2 = 0$. On the other hand, in order to enforce $\tilde{\phi}'(r = b) = 0$ one obtains the relation

$$C_1 = -\,\frac{b\,\pi}{2\,k^2}\,. \tag{29}$$

Hence, for the spherical-well potential one has

$$\tilde{\phi}'(r) = \sqrt{\frac{k^3}{2\,\pi^2}}\Big[\left(\frac{r}{2\,k^2} - \frac{\pi^2}{2\,k^4\,r}\right)\cos(k\,r) + \frac{\pi^2}{2\,k^5 r^{\,2}}\sin(k\,r)\Big] \tag{30}$$

or, equivalently:

$$f(r) = \left(\frac{r^2}{2\,k} - \frac{\pi^2}{2\,k^3}\right)\tan^{-1}(k\,r) + \frac{\pi^2}{2\,k^4\,r} \tag{31}$$

This allows us to finally compute the ground state static polarizability through Eq. (5)

$$\alpha_0 = \frac{4\pi^2 + 3}{12k^2} \tag{32}$$

In the spirit of making an explicit comparison between our, exact theory and an already existing theoretical framework, we can take the VV09 functional (see Appendix), which provides a straightforward integral expression for the ground state polarizability, directly comparable with our model. For the sake of a better, more pronounced comparison of the differences between our theory and VV09, we show the integral kernels employed to compute the ground state polarizability.

From Eq.(5), after an integration over the angular coordinates, it is straightforward to extract the exact (angle-averaged) polarizability functional in terms of the $f(r)$ function:

$$\alpha_{\,\mathrm{exact}}(r) = \frac{2}{3} r\, f(r)\, \rho_0(r) \tag{33}$$

where $\rho_0(r)$ is the ground state density and

$$\alpha_0 = \int d^3r \, \alpha_{\,\mathrm{exact}}(r)$$

It is worth to point out that given the integral formulation of α_0, the definition of $\alpha_{\mathrm{exact}}(\mathbf{r})$ is non-unique, due to an underlying gauge-invariance [45] based on the addition of any regular function with vanishing integral over the entire space [13]. This implies that $\alpha_{\,\mathrm{exact}}(r)$ actually represents a meaningful quantity to be compared and discussed, since any additional angular term in $\alpha_{\mathrm{exact}}(r)$ characterized by angular components different from the one already consider, would not contribute to the radial distribution, since they would simply vanish after angular integration. Thus, we refer to the *exact* functional, as the functional whose integration over the space leads to the correct value of the static ground state polarizability α_0. As it can be seen in Fig. 1, Fig. 2 and Tab. 1 respectively, substantial differences regarding the radial dependencies of the exact and VV09 integration kernels arise, reflecting an important gap when it comes to integrated polarizabilities as well (Tab. 2)

	$f(r)$	$\rho_0(r)$	$\alpha_{\mathrm{VV09}}(r)$
H	$r^2/2 + r$	e^{-2r}/π	$\frac{1}{4\pi}\frac{4e^{-2r}}{4e^{-2r}/3+0.1424}$
QHO	$\frac{r}{\omega_0}$	$\left(\frac{\omega_0}{\pi}\right)^{3/2} e^{-\omega_0 r^2}$	$\frac{1}{4\pi}\frac{4\omega_0^{3/2}e^{-\omega_0 r^2}}{4\omega_0^{3/2}e^{-\omega_0 r^2}/3+\sqrt{\pi}*0.1424\omega_0^4 r^4}$
SW	$\left(\frac{r^2}{2k} - \frac{\pi^2}{2k^3}\right)\tan^{-1}(kr) + \frac{\pi^2}{2k^4 r}$	$\frac{k^3}{2\pi^2}\left(\frac{\sin(kr)}{kr}\right)^2$	$\frac{1}{4\pi}\frac{\frac{2k\sin^2(kr)}{\pi r^2}}{\frac{2k\sin^2(kr)}{3\pi r^2}+0.1424\left(k\tan^{-1}(kr)-\frac{1}{r}\right)^4}$

Table 1: The *exact* $f(r)$ operator ($F(r,\theta) = f(r)\cos(\theta)$) defining the *exact* polarizability functional (i.e. $\alpha_{\mathrm{exact}}(r) = 2rf(r)\rho_0(r)/3$) is reported for Hydrogen, and for an electron immersed in a harmonic potential (QHO, having frequency ω_0), and in a spherical well (SW) with infinite depth and radius b (which defines $k = \pi/b$). The ground-state density is given for reference. Finally, the VV09 polarizability functional $\alpha_{\mathrm{VV09}}(r)$ is also given for comparison.

For hydrogen VV09 exhibits the correct exponential scaling at large r, which directly

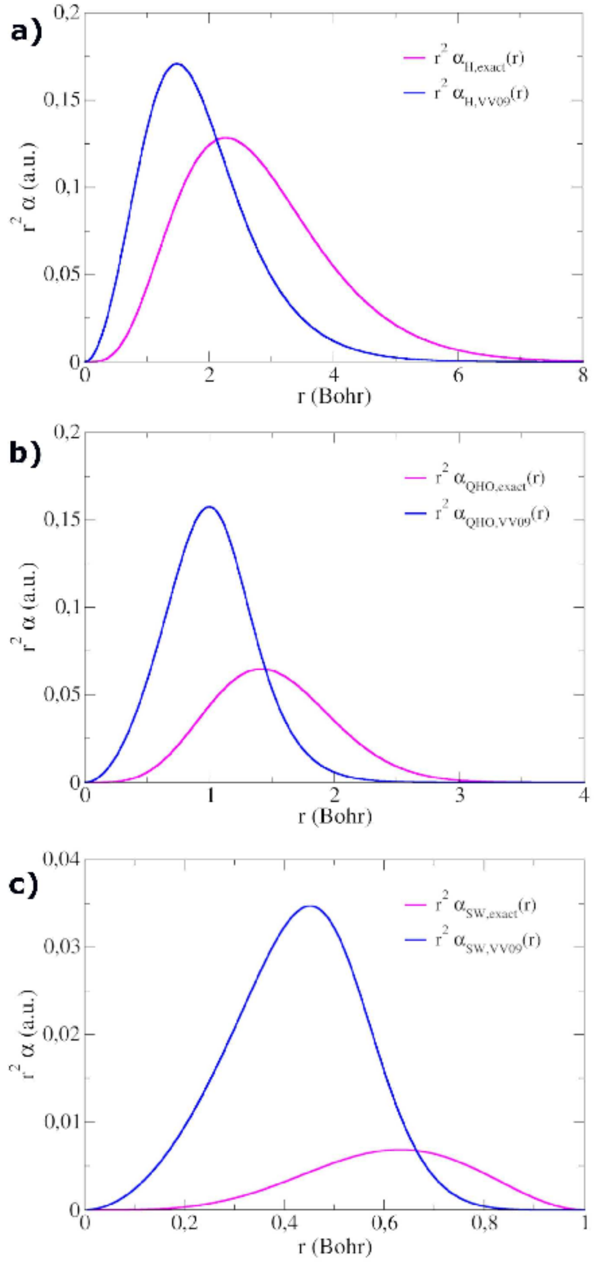

Figure 1: Comparison between exact and VV09 polarizability density functionals α (integrated over angular coordinates) as a function of the radius r, and rescaled by the radial integration weight r^2 for H, QHO ($\omega_0 = 1$a.u.) and S-W ($b = 1$a.u.).

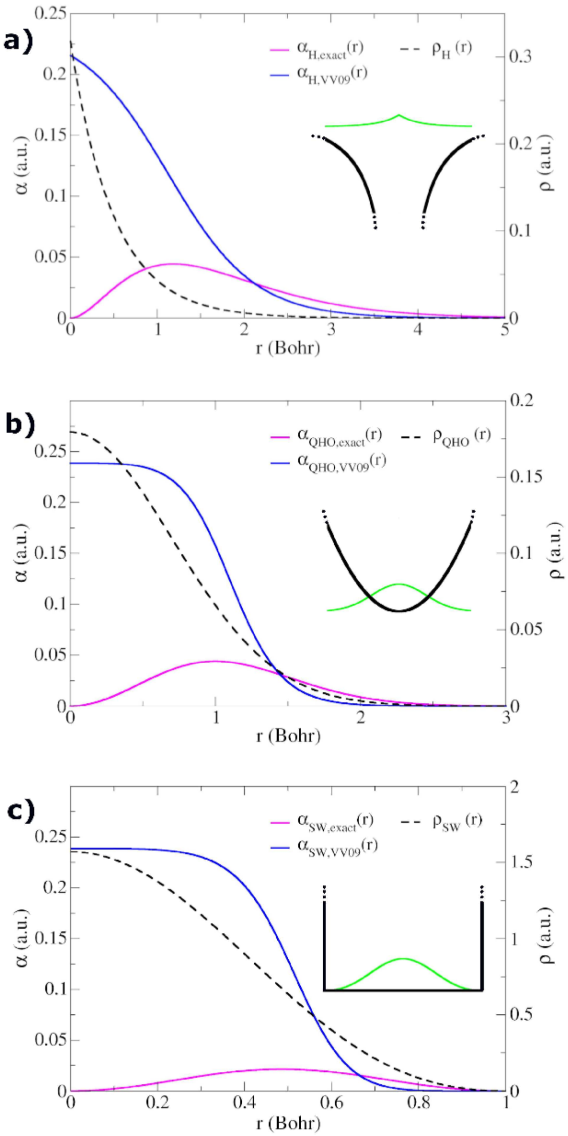

Figure 2: Comparison between exact and VV09 polarizability density functionals α (integrated over angular coordinates) as a function of the radius r, for H, QHO ($\omega_0 = 1$a.u.) and SW ($b = 1$a.u.). electron densities are also reported for comparison. Insets give a pictorial representations of the confining potentials (solid black) and the corresponding electron densities (green).

	Parameter	α_0^{VV09}	α_0
H	a_0		
	1.0	4.24	4.50
QHO	ω_0		
	0.1	84.3	100.0
	1.0	1.72	1.0
	5.0	0.11	0.04
SW	b		
	1.0	0.15	0.036
	5.0	29.09	22.71
	10.0	274.4	363.4

Table 2: Comparison between VV09 and exact static polarizabilities (a.u.) for the considered systems. In QHO and SW the parameters of the potential (ω_0 and b, respectively - given in a.u.) are varied in order to reveal the polarizability scaling. Exact polarizabilities are computed according to the formulas reported in Tab. 1.

stems from the electron density. However, the polynomial factor ($rf(r) = r^3/2 + r^2$) present in our *exact* polarizability functional is essentially missing in the VV09 functional. This causes some overestimation of the polarizability functional at small r (in fact, $\alpha_{\text{exact}}(r)$ tends to zero when $r \to 0$), and implies a slightly different long-range decay (see Fig, 2) [13].

Analogous considerations hold for the QHO, where again the Gaussian scaling deriving from the density distribution is respected, but the polynomial factor is missing. The SW scenario is complicated here by the non-exponential density decay, and by the co-existence of non-polynomial oscillatory factors.

Concerning VV09 static polarizability estimates, one obtains very accurate values for hydrogen ($\alpha_0^{\text{VV09}} \sim 4.24$ a.u.) and a reasonable estimate for QHO with $\omega_0 = 1$ Ha ($\alpha_0^{\text{VV09}} \sim$1.72 a.u., to be compared with α_0^{VV09} 1 a.u. - see Tabs. 1,2). The overestimation of $\alpha_{\text{VV09}}(r)$ at short r seen in Fig. 2 is mitigated by the small integration weight in spherical coordinates: in fact, $r^2\alpha_{\text{VV09}}(r)$ tends to 0 when $r \to 0$.

However, the scaling of the polarizability with respect to ω_0 is not well reproduced by

VV09: α_0^{VV09} passes from ~ 0.11 a.u. at $\omega_0 = 5$ Ha to ~ 84.3 at $\omega_0 = 0.1$ (whereas α_0 goes from $4 * 10^{-2}$ to 10^2 a.u.). Worse performance is found in the short-ranged SW potential, where VV09 overestimates polarizabilities at $b = 1$ Bohr, but the agreement improves when $b = 5$ Bohr due to a slower density decay. Overall, we thus conclude that VV09 is best suited for atomic systems, for which it was explicitly designed.

2.2 van der Waals Density Functional

DFT as an alternative to the ab initio quantum chemistry methods has become the most used method for electronic structure calculations. Such an appreciation of DFT stems from its low computational complexity and the very reasonable accuracy, which is determined by the approximation to the exchange-correlation energy functional E_{xc}. The simplest DFT formulation of the exchange-correlation energy functional is the local density approximation (LDA), where

$$E_{\mathrm{xc}}[n]^{\mathrm{LDA}} = \int \phi[n(\mathbf{r})]$$

where the kernel $\phi(n(\mathbf{r})$ is chosen to reproduce the exactly known energy of the uniform electron gas.

The LDA has been a very successful approximation for many systems of interest, especially those where the eletronic density is quite uniform such as bulk metals, but also for less uniform systems such as molecules, semiconductors, and ionic crystals. There are, however, a number of features that the LDA fails to reproduce: the most dramatic being the following:

- The LDA has a tendency to overestimate the exchange energy and underestimate the correlation energy. However, the errors in the evaluation of the exchange and correlation parts usually tend to compensate each other to a certain degree, leading to surprisingly good result in a wide range of systems.

- Electronic densities of atoms in the core region, where the electrons are strongly localized, are poorly described: the reason is that LDA fails to cancel the self-interaction, which is important for strongly localized states. To the other side, the electronic density in the valence region of the atom is much better reproduced, although it still decays into the vacuum with an incorrect behavior.

- Effects due to truly non local correlation effects, such as the vdW corrections, are not accounted for within LDA.

An enhanced version of the LDA approach is the Generalized Gradient Approximation (GGA) which is able to correct for the tendency of LDA to overestimate the exchange energy and underestimate the correlation one. The GGA strategy consists in accounting for the gradient of the density, leading to a better description of the non-homogeneity of the true electron density of a given system. The semi-local GGA exchange-correlation functional can be written as

$$E_{\mathrm{xc}}^{\mathrm{GGA}}[n] = \int d\mathbf{r}\, n(\mathbf{r})\phi[n(\mathbf{r})]F_{xc}^{GGA}[s(\mathbf{r})]$$

where F is the so called enhancement factor and $s(\mathbf{r})$ is the dimensionless reduced gradient:

$$s(\mathbf{r}) = \frac{1}{2\pi^2 n(\mathbf{r})}\frac{|\nabla n(\mathbf{r})|}{n(\mathbf{r})}$$

note that when $|\nabla n(\mathbf{r})| \to 0$, then $s(\mathbf{r}) \to 0$ and the function F is chosen so that, within these conditions $F \to 1$ the LDA is fully recovered. The GGA approach, whose most famous implementation is the one from Perdew–Burke–Ernzerhof [17] has brought considerable improvements in the electronic description of non-uniform system characterized by strong, covalent bonding, even though it remains inadequate for a wide range of interesting physical systems. In fact, the GGA fails, exactly as the LDA, in the description of non-local correlation effects, which are fundamentals in a wide class of interesting systems. One of the most important and ubiquitous non-local effects relies in the dispersion, long-range vdW interactions, whose accurate description stands out as one of the most crucial issues in modern DFT [16]. In the last decades, huge efforts have been put into addressing a proper description of non-covalent London dispersion forces [19, 20, 21]. Multiple vdW techniques were proposed [22, 23, 24, 25, 26, 10, 27, 28], which enabled efficient description of interfaces and nanostructures [21, 29, 30, 31, 32, 33, 34], molecular crystals [35, 36] and biomolecules [37]. Among these, self-consistent vdW approaches [19, 39, 11, 40, 41, 38] exploit explicitly non-local correlation functionals, coherently with the DFT framework. Popular Chalmers/Langreth-Lundqvist [19] (LL) and Vydrov-van Voorhis [11] (VV) non-local vdW functionals obtain a two-point dependence [42] on the groundstate electron density $\rho_0(\mathbf{r})$:

$$E_{\mathrm{vdW}}\left[n\right] = -\int d^3r_1 d^3r_2 \phi(n(\mathbf{r}_1), n(\mathbf{r}_2), \mathbf{r}_1, \mathbf{r}_2)\,. \tag{34}$$

Here ϕ scales as $|\mathbf{r}_1 - \mathbf{r}_2|^{-6}$ at large distance, compatibly with pairwise Lennard-Jones potentials for pointlike fragments, and its explicit form is obtained from a Casimir-Polder integral, upon introduction of a (semi-)local polarizability functional $\alpha(\mathbf{r})$, from which the polarizability densities at $\mathbf{r}_1$ and $\mathbf{r}_2$ are computed. To date, benchmarking of such functionals has been done via extensive higher-level numerical energy estimations. Hereafter, following the same approach as for the polarizability functional, we derive a general theoretical framework [13] and exact expressions for the vdW density functionals as well, exploiting a solution for the same physical systems treated in the previous section. Direct comparison with available vdW density functionals are made, providing solid theoretical foundation for the two-point integral kernel ϕ, in small, weakly interacting systems, and enabling direct insights in long-range electron correlation.

Consider two isotropic atoms with N_1 and N_2 electrons respectively, separated by a large distance R. The Hamiltonians and energy eigenstates of the isolated atoms obey $\hat{H}_1|n_1\rangle = E_{n1,1}|n_1\rangle$ and $\hat{H}_2|n_2\rangle = E_{n2,2}|n_2\rangle$. The combined electronic states are spanned by product states $|n_1n_2\rangle$. The asymptotic inter-atomic vdW interaction energy is $E_{vdW} = -C_6R^{-6}$ where, from second-order perturbation theory

$$C_6 = \sum_{\substack{n_1\neq 0_1\\ n_2\neq 0_2}} 6\frac{\langle 0_10_2|\hat{D}_{z,1}\hat{D}_{z,2}|n_1n_2\rangle\langle n_1n_2|\hat{D}_{z,1}\hat{D}_{z,2}|0_10_2\rangle}{(E_{n1,1}-E_{0,1})+(E_{n2,2}-E_{0,2})}\,. \tag{35}$$

Here $\hat{D}_{z,1} = -|e|(z_{1,1}+z_{2,1}+...+z_{N,1})$ and $\hat{D}_{z,2} = -|e|(z_{1,2}+z_{2,2}+...+z_{N,2})$ are the dipole moment operators for the isolated atoms. Eq. (35) can be derived from the standard integral expression [26]

$$C_6 = \frac{3}{\pi}\int_0^\infty \alpha_{0,1}(i\omega)\alpha_{0,2}(i\omega)\,d\omega\,, \tag{36}$$

where $\alpha_{0,1}(i\omega)$ and $\alpha_{0,2}(i\omega)$ are the dynamic dipolar polarizabilities of the two atoms. Substitution of Eq. (4) into Eq. (36) gives

$$\begin{aligned} C_6 = \frac{3}{\pi}\sum_{\substack{n_1\neq 0_1\\ n_2\neq 0_2}}\int_0^\infty d\omega\,\frac{2(E_{n1,1}-E_{0,1})}{(E_{n1,1}-E_{0,1})^2+\omega^2}\frac{2(E_{n2,2}-E_{0,2})}{(E_{n2,2}-E_{0,2})^2+\omega^2}\times \\ \langle 0_10_2|\hat{D}_{z,1}\hat{D}_{z,2}|n_1n_2\rangle\langle n_1n_2|\hat{D}_{z,1}\hat{D}_{z,2}|0_10_2\rangle\,. \end{aligned} \tag{37}$$

Straightforward analytical integration over ω removes the dependence on imaginary frequencies, yielding the exact *static* expression Eq. (35). We remark that Eq. (36) is one of the most popular way to predict C_6, but it is usually combined with an approximate evaluation of the $A(i\omega)$ e.g. from time dependent density functional theory [46]. Instead, here we will show how to evaluate C_6 exactly using neither frequency integrations, nor explicit excited-state sums as in Eq. (35) [13]. To this end, similarly to the derivation of the polarizability functional above, we introduce an operator $\hat{F}_{12}$ with the property

$$\langle n_1 n_2|\hat{F}_{12}|0_1 0_2\rangle = \frac{\langle n_1 n_2|\hat{D}_{z,1}\hat{D}_{z,2}|0_1 0_2\rangle}{(E_{n1,1} - E_{0,1}) + (E_{n2,2-E_{0,2}})} \,. \tag{38}$$

Then (35) becomes

$$C_6 = 6 \sum_{\substack{n_1 \neq 0_1 \\ n_2 \neq 0_2}} \langle 0_1 0_2|\hat{D}_{z,1}\hat{D}_{z,2}|n_1 n_2\rangle\langle n_1 n_2|\hat{F}_{12}|0_1 0_2\rangle - 6\langle 0_1 0_2|\hat{D}_{z,1}\hat{D}_{z,2}|0_1 0_2\rangle\langle 0_1 0_2|\hat{F}_{12}|0_1 0_2\rangle \,. \tag{39}$$

Using the sum-rules (completeness relations) $\sum_{n1} |n_1\rangle\langle n_1| = 1$ and $\sum_{n2} |n_2\rangle\langle n_2| = 1$, and noting that $\langle 0_1 0_2|\hat{D}_{z,1}\hat{D}_{z,2}|0_1 0_2\rangle = 0$ by symmetry for isotropic atoms, we reduce the last equation to the exact result

$$C_6 = 6\langle 0_1 0_2|\hat{D}_{z,1}\hat{D}_{z,2}\hat{F}_{12}|0_1 0_2\rangle \,. \tag{40}$$

We now show how to obtain $\hat{F}_{12}$ exactly by solving a differential equation. In Eq. (38) multiplication through by the energy denominator gives

$$[(E_{n1,1} - E_{0,1}) + (E_{n2,2} - E_{0,2})]\langle n_1 n_2|\hat{F}_{12}|0_1 0_2\rangle = \langle n_1 n_2|\hat{D}_{z,1}\hat{D}_{z,2}|0_1 0_2\rangle \,. \tag{41}$$

Since $E_{n1,1}\langle n_1 n_2| = \langle n_1 n_2|\hat{H}_1,\ E_{0,1}|0_1 0_2\rangle = \hat{H}_1|0_1 0_2\rangle$ and similarly for $\hat{H}_2$, the last equation can be written

$$\langle n_1 n_2|\hat{H}\hat{F}_{12} - \hat{F}_{12}\hat{H}|0_1 0_2\rangle = -\langle n_1 n_2|\hat{D}_{z,1}\hat{D}_{z,2}|0_1 0_2\rangle \,, \tag{42}$$

where $\hat{H} = \hat{H}_1 + \hat{H}_2$. This in turn is satisfied if

$$[\hat{H}, \hat{F}_{12}]|0_1 0_2\rangle = \hat{D}_{z,1}\hat{D}_{z,2}|0_1 0_2\rangle \,. \tag{43}$$

The groundstate-projected commutation relation (43) can have many solutions for $\hat{F}_{12}$, since we can add any operator $\hat{G}$ such that $\hat{G}|0_1 0_2\rangle = 0$ [13]. We exploit this freedom to discover that solutions exist where $\hat{F}_{12}$ is a local and multiplicative operator so that $(\hat{F}_{12}\psi)(\mathbf{X}) = F_{12}(\mathbf{X})\psi(\mathbf{X})$ for any many-electron wavefunction $\psi(\mathbf{X})$ of the two-atom system. Here $\mathbf{X} = (\mathbf{X}_1; \mathbf{X}_2) = (\mathbf{r}_{1,1}, \mathbf{r}_{2,1}, ..., \mathbf{r}_{N,1}; \mathbf{r}_{1,2}, \mathbf{r}_{2,2}, ..., \mathbf{r}_{N,2})$ is the many-electron position variable for the combined system of $(N_1 + N_2)$ electrons. Since the Hamiltonian $\hat{H} = \hat{H}_1 + \hat{H}_2$ is a differential operator in the $\mathbf{X}$ space, Eq. (43) is a single multi-dimensional differential equation for the function $F_{12}(\mathbf{X})$, with input from the two atomic groundstate wavefunctions $\psi_{0,1}(\mathbf{X}_1) = \langle \mathbf{X}_1|0_1\rangle$ and $\psi_{0,2}(\mathbf{X}_2) = \langle \mathbf{X}_2|0_2\rangle$. Once F_{12} is found, the vdW C_6 coefficient is evaluated exactly via a spatial integration as specified in Eq. (40). Since the vdW interaction is proportional to the C_6 coefficient, and R is a fixed parameter, one automatically obtains the vdW density functional.

2.2.1 H dimer

Here $N_1 = N_2 = 1$ and $\hat{D}_{z,i} = -z_i$ $(i = 1, 2)$ in atomic units. Then (40) becomes

$$\Big[-\frac{1}{2}(\nabla_1^2 + \nabla_2^2), F_{12}(\mathbf{r}_1, \mathbf{r}_2)\Big]\psi_{0,1}(\mathbf{r}_1)\psi_{0,2}(\mathbf{r}_2) = z_1 z_2 \psi_{0,1}(\mathbf{r}_1)\psi_{0,2}(\mathbf{r}_2)\,. \tag{44}$$

Since $z_1 z_2 = r_1 r_2 \cos\theta_1 \cos(\theta_2)$ and $\psi_{0,1}(\mathbf{r_1})\psi_{0,2}(\mathbf{r_2}) = \psi_{0,1}(r_1)\psi_{0,2}(r_2)$ in polar (r, θ, ϕ) coordinates, the last equation has a solution of the form

$$F_{12}(\mathbf{r_1}, \mathbf{r_2}) = f_{12}(r_1, r_2)\cos\theta_1 \cos\theta_2\,. \tag{45}$$

In the case of H atoms, Eq. (44) is rearranged into

$$-\partial_{r_1}^2 f_{12} - 2\left(\frac{1}{r_1} - 1\right)\partial_{r_1} f_{12} + \frac{2}{r_1^2} f_{12} + -\partial_{r_2}^2 f_{12} - 2\left(\frac{1}{r_2} - 1\right)\partial_{r_2} f_{12} + \frac{2}{r_2^2} f_{12} = 2 r_1 r_2\,. \tag{46}$$

The analytic solution of this equation is unknown. However, a rapidly converging numerical approach is possible [47, 13]. One can now define $f_{12} = -2 r_1 r_2 \tilde{f}_{12}$. Then, by introducing the change of variables $\xi_1 = 2r_1$ and $\xi_2 = 2r_2$ one obtains

$$\frac{\partial^2 \tilde{f}_{12}}{\partial \xi_1^2} + \frac{\partial^2 \tilde{f}_{12}}{\partial \xi_2^2} + \left(\frac{4}{\xi_1} - 1\right)\frac{\partial \tilde{f}_{12}}{\partial \xi_1} + \left(\frac{4}{\xi_2} - 1\right)\frac{\partial \tilde{f}_{12}}{\partial \xi_2} - \left(\frac{1}{\xi_1} + \frac{1}{\xi_2}\right)\tilde{f}_{12} = \frac{1}{4} \tag{47}$$

One can now expand $\tilde{f}_{1,2}$ into Laguerre polynomials as follows:

$$\tilde{f}_{12} = -\sum_{l,n} a_{ln} L^3_{n-2}(\xi_1) L^3_{n-2}(\xi_2)\,, \tag{48}$$

obtaining the equation

$$\sum_{l,n} a_{ln}\left(\frac{l-1}{\xi_1} + \frac{n-1}{\xi_2}\right) L^3_{l-2}(\xi_1) L^3_{n-2}(\xi_2) = -\frac{1}{4}\,. \tag{49}$$

This equation can be multiplied on both sides by

$$\xi_1^4 \xi_1^4 e^{-\xi_1} L^3_{m-2}(\xi_1) e^{-\xi_2} L^3_{s-2}(\xi_2)$$

Then, after performing integration and using the properties of Laguerre polynomials, the following infinite set of recursive equation for the a_{nl} coefficient can be derived [47]:

$$-a_{n,l}\,(2\,l\,g_n\,q_l + 2\,n\,g_l\,q_n) + a_{n,l-1}\,(l+1) g_n\,q_{l-1} + a_{n,l+1}\,(l-1) q_n\,q_{l+1} + \tag{50}$$

$$a_{n-1,l}\,(n+1) g_l\,q_{n-1} + a_{n+1,l}\,(n-1) g_l\,q_{n+1} = \Delta_{n,l} \tag{51}$$

where

$$g_n = \frac{1}{144}\frac{(n-1)(n+1)!}{(n-2)!} \;\;,\;\; q_n = \frac{(n+1)!}{(n-2)!}$$

and

$$\Delta_{n,l} = \delta_{n,2}\delta_{l,2} - \delta_{n,3}\delta_{l,2} - \delta_{n,2}\delta_{l,3} + \delta_{n,3}\delta_{l,3}$$

which can be symbolically solved truncating the summation in Eq.(48) [13] at the required convergence threshold for the n, l indexes. This will give an actual expression for $\tilde{f}_{1\,2}$, which can be used to compute the C_6 coefficient directly from the integral (37). Note that it is implicitly assumed that problem is symmetric, which means that the matrix a_{nl} is symmetric (ie. $a_{nl} = a_{ln}$). In table 3 we report the computed C_6 coefficient as a function of the truncation order, which shows fast convergence towards the well-known exact value of 6.5 a.u.

Truncation Order	C_6 (a.u.)
0	6.00000
1	6.46154
2	6.49813
3	6.49896
4	6.49902
5	6.49903

Table 3: computed C_6 coefficient for the H-dimer as a function of the summation truncation order. This latter is defined as the highest power the Laguerre polynomials. For example, at order 0, the f_{ab} used for the C_6 computation reads:
$f_{ab} = a_{00}L_0^3(r_a)L_0^3(r_b) = f_{00}$, while at order 1 we have: $f_{ab} = [f_{00} + f_{10} + f_{01}](r_a, r_b)$.

2.2.2 Quantum Harmonic Oscillators

In the case of two quantum harmonic oscillator coupled by a dipolar interaction, differently from the previous case, we will exploit a simple and elegant analytical solution. It is worth to point out that QHOs systems are of high relevance in condensed matter computational physics, since it has been demonstrated [52] that for a system of QHOs coupled through a dipole-dipole potential there is an equivalence between the full interaction energy obtained from the Hamiltonian diagonalization and the ACFD-RPA correlation energy. This proof has huge impact from the computational point of view, being the time complexity of a standard RPA calculation $\sim O(N^5)$ for a system of N electrons, while matrix diagonalization on the same system has a much lower time complexity (N^3). The above argument is indeed one of the foundations for the Many Body Dispersion[27] (MBD) method, which models atom as QHOs and is able to predict highly accurate vdW interaction energies at the computational cost of a matrix diagonalization. That being said, deriving an exact expression for the C_6 coefficient of a simpler system consisting of two interacting QHOs contributes to a better understanding of the disperion forces modelization.

The Hamiltonian for a system of two 3D harmonic oscillator of frequencies ω_1 and ω_2 interacting via dipole-dipole interactions has the following form:

$$H = -\frac{1}{2}\sum_{i=1}^{2}\frac{\nabla^2_{\mathbf{r_i}}}{m_i} + \frac{1}{2}\sum_{i=1}^{2} m_i\omega_i^2\mathbf{r_i}^2 + \omega_1\,\omega_2\,\sqrt{\alpha_1\alpha_2}\,\mathbf{r_1}\,\mathbf{T_{12}}\,\mathbf{r_2}$$

The interaction energy in the Hamiltonian above has been written in terms of the dipolar tensor T and the static polarizabilities $\alpha_{1,2}$ of the two isolated oscillators (having characteristic frequency $\omega_{1,2}$). Finally, the charge of each QHO has been put $q_{1,2} = 1$ and we choose $m_1 = m_2$ an $\omega_1 = \omega_2 = \omega_0$ for the sake of simplicity. Hereafter we assume the QHOs to be displaced along the z axis, so that the only non-zero component of the dipolar tensor is $T_{12}^{zz} = -2/R^3$ and the 3D Hamiltonian is equivalent to

$$H = -\frac{1}{2m}\nabla_1^2 + \frac{1}{2}m\omega_0^2 r_1^2 - \frac{1}{2m}\nabla_2^2 + \frac{1}{2}m\omega_0^2 r_2^2 - \frac{2}{R^3}\,z_1\,z_2$$

Similarly to what has been done for the case of the polarizability functional, it is possible to rewrite Eq.43 as

$$(E_0 - H_0)F_{12}\psi_0 = H_{\text{int}}\psi_0\,, \tag{52}$$

where $H_{int} = -2/R^3$. The ground state wave function for the non interacting system is

$$\psi_0(r_1, r_2) = \left(\frac{m\omega_0}{\pi}\right)^{3/2} e^{\frac{m\omega_0 r_1^2}{2}} \, e^{\frac{m\omega_0 r_1^2}{2}}$$

and the ground state energy is $E_0 = -3\omega_0$. Assuming now the operator F to have the same shape as the one of Eq. 45, substituting into Eq. 52, one obtains the following differential equation:

$$\left[\partial_{r_1}^2 + \partial_{r_2}^2 + \sum_{i=1}^{2} \left(\frac{4}{r_i} - 2\, m\, \omega_0\, r_i\right) \partial_{r_i} - 16\, m\, \omega_0\right] f(r_1, r_2) = 3\, m\, \omega_0$$

whose analytical solution is:

$$f(r_1, r_2) = \frac{r_1\, r_2}{2\, \omega_0} \tag{53}$$

at this point, we can compute the integral of Eq.(37), which leads to the exact C_6 value:

$$C_6 = \frac{3}{4\omega_0^3}$$

which matches with the results given in Ref. [64].

We do not explicitly report the procedure carried out for the case of two particles confined in a spherical-well potential, which can be achieved following the exact same procedures presented in this sections.

Since direct implications beetween energetics and C_6 coefficient exist, it is worth to perform an explicit comparison between our, exact model for vdW energy functionals, and the VV09 results (see (56) in the Appendix). From Eq.(40), without losing of generality, we can extract the integral kernel which leads to the correct C_6 values as:

$$\phi_{\mathrm{exact}}(r_1, r_2) = \frac{6}{R^6}\, n(r_1)\, n(r_2)\, r_1\, r_2\, f_{12}(r_1, r_2) \cos(\theta_1) \cos(\theta_2)$$

Note that also in this case the functional inherits the gauge arbitrariness already discussed for the polarizability functional, so we can neglect the angular dependencies while comparing the two theoretical models.

First, we note that both *exact* and VV09 functionals show analogous two-point integral dependency on $\mathbf{r}_1$, $\mathbf{r}_2$. Unlike ϕ_{VV09} (see Appendix.), our ϕ_{exact} depends implicitly on $\rho_0(\mathbf{r})$ at all space points $\mathbf{r}$, not just $\mathbf{r}_1$, and $\mathbf{r}_2$. Moreover, according to perturbation theory, three-point functional terms should be further introduced when addressing three one-electron fragments (and more points should appear in larger clusters). As from Fig. 3, within our gauge of choice, VV09 overestimates ϕ at short distance, while showing qualitatively similar decay at the long range, where densities are rapidly vanishing. We also note the rather different scales that characterize VV09 and *exact* vdW functionals. The quasi-globular shapes of the *exact* functionals stem from the polynomial factors also present in the *exact* polarizability functionals. Also in this case exact and numerical (VV09) C_6 Hamaker coefficients can be directly computed. For atomic H the approximate $C_{6,\mathrm{VV09}} \sim 6.2$ a.u. compares favourably with the exact value $C_{6,\mathrm{exact}} \sim 6.5$ a.u. in spite of the different functional form. We recall that radial integration can smooth out the differences reported in Fig. 3, hiding qualitative discrepancies - multiplication of the VV09 functional by radial weights $r_1^2 r_2^2$ would also produce quasi-globular plots, regardless of the different polynomial dependence. Coming to the QHO ($\omega_0 = 1$ a.u.), $C_{6,\mathrm{VV09}}$ amounts to ~ 1.63 a.u., which is larger than the

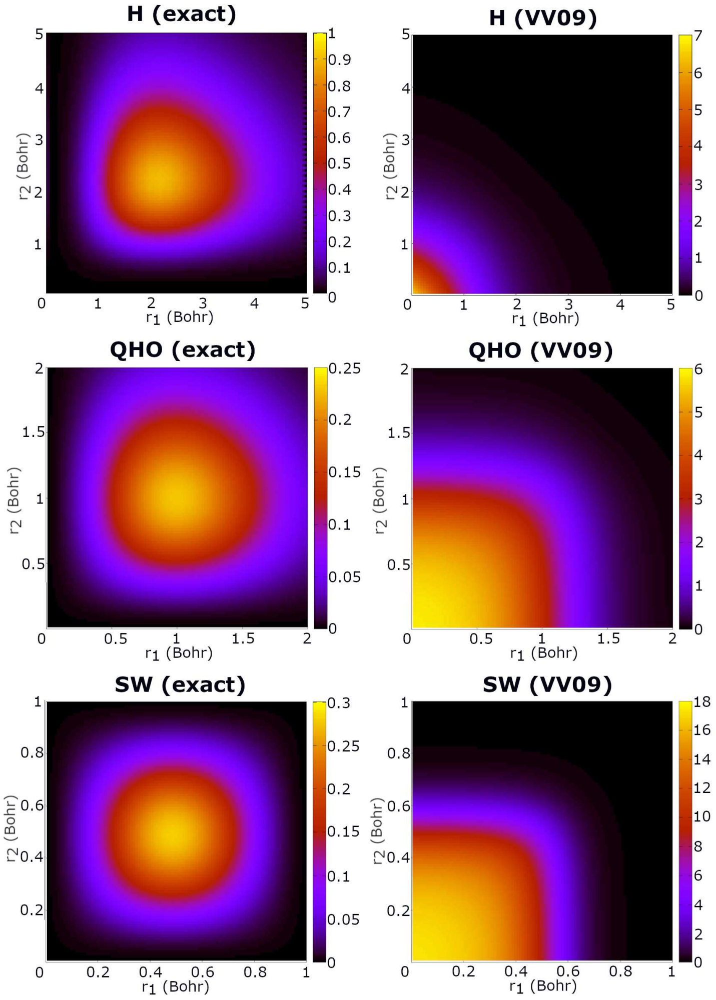

Figure 3: Comparison between exact and VV09 polarizability density functionals α (integrated over angular coordinates) as a function of the radius r, and rescaled by the radial integration weight r^2 for H, QHO ($\omega_0 = 1$a.u.) and S-W ($b = 1$a.u.).

exact value 0.75 a.u. In the strongly-confined SW system ($b = 1$ Bohr), VV09 predicts $C_{6,\mathrm{VV09}} \sim 3.9 * 10^{-2}$, i.e. almost an order of magnitude larger than the corresponding exact result, namely $\sim 5.1{*}10{-}3$ a.u. The final performance of VV09 energetics accordingly depends on the specific system, and it improves when the density decay roughly occurs at atomic scales, as already noted for polarizabilities. In fact, VV09 was mainly designed to address molecular systems, and was benchmarked on structural and energetic data. In multi-atom systems our theory could be extended via pairwise atomic summation, but this approach has known deficiencies for large anisotropic/metallic structures [51, 49, 48, 50, 52, 53, 54, 55, 56, 57, 58].

3 Transition metal dichalcogenides: the case of TiS_2

A particularly interesting class of materials where vdW effects are relevant is represented by the so-called transition metal dichalcogenides (TMDs), which are systems characterized by mild stiffness, not as soft as tissues and not as strong as metals.[65] In a TMD, a transition metal atom (M) layer is sandwiched between two chalcogen atom (X) layers and it is commonly assumed that the MX_2 slabs are stacked by vdW interactions, whereas the intralayer M-X interactions are instead covalent. The weak, interlayer vdW interactions play a key role in the formation, intercalation, exfoliation and layer-by-layer building of TMDs materials, as well as being decisive for their structural and electronic properties.

This section is dedicated to first-principle DFT study of bulk TMDs, meaning that we are interest in a detailed description of the electron density (ED) of the ground state, which is the core quantity in the theoretical framework of DFT. ED fully determines the total energy of any many-electron system and probably represents the most information-rich observable available since it has become possible to determine EDs from analysis of structure factors obtained from accurate X-ray diffraction data. During the past decade, the accuracy of experimental X-ray diffraction data has increased dramatically owing to the use of high-energy synchrotron sources, which significantly limit systematic errors in the data and, thanks to these modern techniques, nowadays it is possible to evaluate both structural and electronic properties of a wide class of layered materials in an extremely accurately way. In this respect, Medvedev *et al.*[67] have pointed out that modern DFT functionals are constructed on the basis of empirical fitting on energetic and geometrical benchmarks, neglecting the ED as a parameterization parameter. If, from one side, this leads to improved predictions of energetic and structural features, from the other, the exact reproduction of the ED has worsened. We will mainly focus on the case of TiS_2, an archetypal vdW material recently investigated by Kasai *et al.*[66] [14]. In this study a detailed analysis on the ground state ED of TiS_2 has been carried out, comparing the ED distribution derived from X-ray diffraction data with the theoretical one obtained by several DFT functionals. They obtained a good agreement between theory and experiment for the description of the intralayer, covalent Ti-S interaction, but, at the same time, significant discrepancies were found for the interlayer vdW interactions, particularly considering the ED distribution in the region between S atoms belonging to adjacent layers. In fact, while the properties at the bond critical point (BCP) were quite similar, noticeable differences were instead observed away from the BCP: considering the theoretical DFT density, the S atoms behave as if they are practically not interacting with the neighboring layer, showing charge concentration and accumulation in the region expected for a lone pair in an *sp3*-hybridized S atom with three bonds to nearby Ti atoms and no other bonds; in the experiment, however, an appreciable charge accumulation and concentration was observed in the interlayer region, which was interpreted as a sign of a stronger and more directional interaction between S atoms. Thus, this study suggested the inability of current DFT functionals to accurately describe the interlayer ED for vdW layered materials, supporting the conclusions of Medvedev *et al.*

This section has the main purpose of deeply investigate the issue described so far [14] and can be divided in two halves. In the first part of the study, we apply different DFT functionals, with standard Projector-Augmented Wave (PAW) pseudopotentials,[76] to explore electronic and energetic behaviors of TiS_2. We will provide extensive benchmarks also artficially tuning the intensity of the vdW interactions for the system of interest, leading to an exhaustive benchmark of both energetic and electronics properties of the system of interest [14]. In the second part a standard rVV10 approach is adopted, but a novel pseudopotential is generated for the purpose of explicitly accounting for the $3d$ orbitals of the S atom [14]. In fact, while these orbitals are empty in the isolated, neutral S atom, it has been pointed out[80] that they can play a role in molecules and condensed-matter systems where S atoms interact with other atoms and form bonds. We will show that, interestingly, using this novel, more flexible S pseudopotential, we obtain not only an ED distribution profile closer to the experimental one provided by Kasai *et al.*, but also a better estimation of the interlayer binding energy (ILBE) [14]. We finally show that this improvement in the theoretical DFT description is not limited to TiS_2 only, but also holds for other, similar TMDs involving S atoms, such as TaS_2 HfS_2, and MoS_2 [14].

3.1 Electronic, Structural and Energetical Benchmarking of TiS_2

In this section a detailed structural, electronic and energetic analysis of TiS_2 is performed. For this purpose, six different density functional schemes are applied, namely the LDA, the semilocal PBE[17] and the vdW-corrected rVV10[12]. In particular, the rVV10 functional is employed both following its standard definition (see Appendix for further details) and also considering three variations, each of them characterized by a different intensity of both long and short range vdW interactions. More specifically, the rVV10($b = 1.0$) model was purposely built to artificially increase the strength of short-range vdW interactions, leaving unchanged the intensity of the long-range component, while the opposite case is explored within the rVV10($b = 10.0$) model, which instead decreases the intensity of the short-range dispersion interaction. Finally, a third models rVV10($b = 1.1$, $C = 0.00207$), named as $\mathrm{rVV10}_{\mathrm{opt}}$, is employed. This latter is characterized by a new value of the C parameter, leading to a modified C_6 coefficient responsible for the long-range behavior of the vdW interactions, and also by a slightly changed b parameter with respect to that of the standard rVV10 (b = 1.0). Finally, we mention that the latter $\mathrm{rVV10}_{\mathrm{opt}}$ has been purposely built a posteriori, looking for an improvement of the ED distribution in the interlayer plane; the results presented below will make clear the reasons behind this choice.

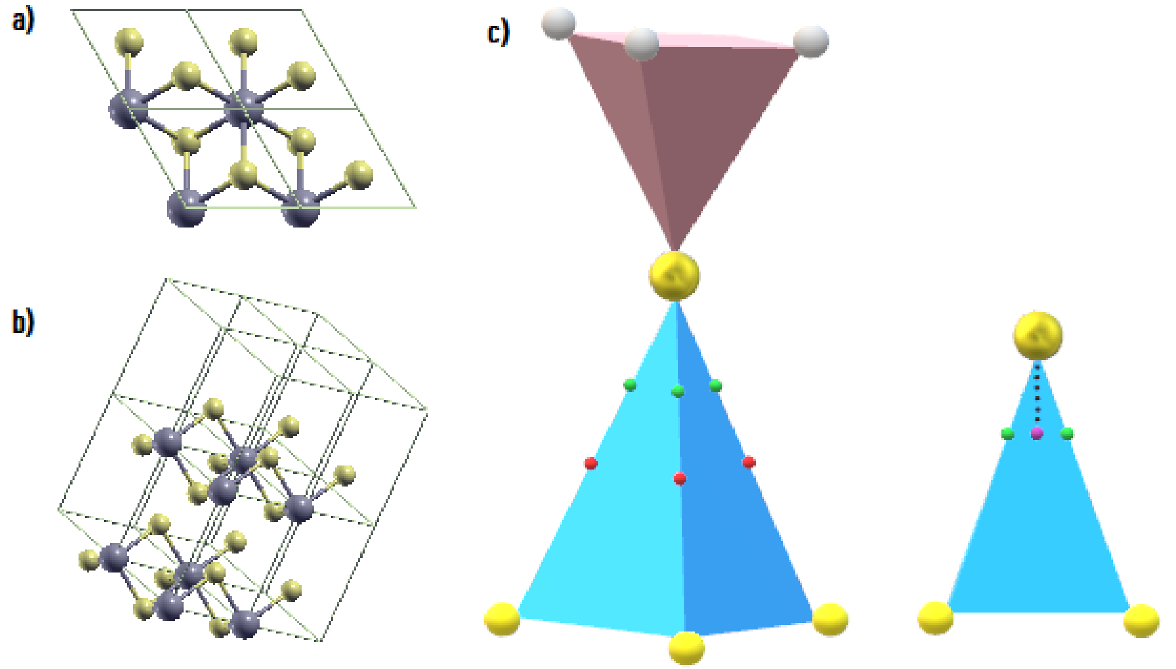

Figure 4: a) & b): bulk structure of TiS_2. The unit cell is repeated twice along the x, y, and z directions. c) On the left hand side the TiS_2 octahedron is represented: the bigger S atom in the middle is the reference S atom, while the grey balls denote Ti atoms. The lower tetrahedron sides indicate the S-S lines, connecting the reference atom to the S atoms belonging to the adjacent layer. On the right hand side, the S-center line (connecting the reference S atom to the center of the lower tetrahedron) is represented by dots. The green spheres denote the positions of the (3, -3) critical points (CPs) along the S-S lines, the red spheres are referred to the (3, -1) CPs and, finally, the violet sphere shown inside the triangular section (right side of the c) panel) represents the position of the (3, -3) CP belonging to the S-center line.

3.1.1 Preliminary Analysis: Energetical and Structural Assessment

First of all, a preliminary analysis of the basic structural and energetical properties of the system has been carried out, also, focusing on two other interesting physical quantity, namely the volume of the atomic basin of the S atom and the total electronic charge belonging to it. This analysis is useful mainly for assessing the correctness of the pseudopotential choice, as well as the other computation details, such as the cutoffs in the plane-wave expansion, furthermore, it will give us useful information regarding the nature of the weaker, vdW chemical bond responsible for the stability of the layered structure of TiS_2.

Our ab-initio calculations have been performed using Quantum ESPRESSO (QE) DFT package.[73, 74] We first used for Ti and S atoms standard PAW[76] pseudopotentials taken from the QE database[75]. Subsequently, for further testing, we have generated, for the S atom, a novel pseudopotential, using the *atomic* QE program. Self-consistent calculations and relaxation processes, leading to the ground-state equilibrium geometry of bulk TiS_2, were carried out within the *PWscf* QE program. The calculations adopted plane-wave and density cutoffs of 100 and 1000 Ry, respectively, to get highly-converged results, a cold-smearing parameter of 0.01 Ry, and a 12×12×4 k-point mesh for the sampling of the Brillouin Zone (BZ). The ED analysis is carried out using the *PostProc* QE program, employing the B-Spline method[77] for the $n(x, y, z)$ interpolation; in particular, in the case of TiS_2, for the ED profile computed along the S-S, S-center, and Ti-S lines, a real-space grid of 600×600×800 (x, y, z) points, generated inside a parallelepiped containing the axis of interest, is used. To get a reliable estimate of the laplacian $\nabla^2 n(\mathbf{r})$ function, in the case of the S-S line, the distance between the parallelepiped axis and the edges of its sides is 0.5 Å, for the S-center case 0.25 Å, and finally 0.35 Å for the Ti-S line. The ED is then processed by using the *Critic2* program[78, 79]. More specifically, we compute the ED charge deformation, $\Delta n(\mathbf{r})$, by considering a spatial mesh of 72×72×108 points inside the unit cell (containing one Ti atom and two S atoms) and taking the difference between the ED $n(\mathbf{r})$ and the sum of the EDs of the isolated Ti and S atoms. $\Delta n(\mathbf{r})$ profiles and Laplacian $\nabla^2 n(\mathbf{r})$ maps, in the interlayer and intralayer areas, are then evaluated on the plane of interest using *Critic2*. The calculation of the atomic properties of a given S atom is carried out by making an integration of the so-called ”atomic basin” of the S atom, represented by the space region whose surface has zero-density gradient flux. This is done again with the

Critic2 program, that allows to compute spherical multipolar moments defined as

$$Q_{lm} = \int_A n(\mathbf{r})\, r^l\, Y_{lm} \tag{54}$$

where the integration domain A is the atomic basin volume. In the above equation, $n(\mathbf{r})$ is the charge ED and Y_{lm} are the spherical harmonics, in which the m index runs over the interval [-l ; l]. With this definition, the magnitude of the dipole moment attributed to the S atom is obtained as the square root of the sum of the squared l=1 terms:

$$d(q_A) = \sqrt{\sum_{m=-1,0,1} Q_{1m}^2}\ . \tag{55}$$

We prepared a TiS_2 bulk structure starting from the experimental lattice parameters, a = 3.398 Å and c = 5.665 Å, as reported by Kasai *et al.*,[66]. Employing the presented functional schemes with standard PAW pseudopotentials, we relaxed the intralayer atomic plane of the structure until the force acting on the system was smaller than 10^{-5} Ry/a.u. This relaxation process of the intralayer plane, leads to very similar results for all the adopted functionals: this does not come as a surprise, since vdW interactions do not substantially influence the geometry of the intralayer plane [66]. The structural analysis concerning the interlayer relaxation is instead of relevant physical interest, being clear that the longitudinal lattice constant c is strongly influenced by the effect of dispersion forces. Subsequently, we performed a benchmarking of basic energetics quantity, such as the interlayer binding energy (ILBE) and the cohesive energy of the atomic basis (CE) as well, and, finally, an estimation of the atomic basic volume and its charge is given. All the results of this analysis are reported in Table 4.

Optimizing the interlayer lattice constant c for each functional adopted (third column of Table 4), we obtained results close to the experimental reference values using the rVV10 and rVV10(b=10.0) functionals, with an error of only ~ 3 %. Instead, the quality of the PBE, rVV10(b=1.0), and LDA estimates is worse, with PBE that substantially overestimates, and LDA and rVV10(b=10.0) which instead underestimate. This behavior does not come as a surprise: in fact LDA and the semilocal PBE functional are not able to properly describe the vdW interactions, while the rVV10(b=1.0) functional was deliberately built to artificially increase the strength of short-range vdW interactions, thus leading to a larger interlayer bonding energy and to a shorter layer-layer distance. The CE is defined as E(TiS_2) - E(Ti) - 2E(S), where E(TiS_2) is the total energy of the TiS_2 atomic basis, while E(Ti) and E(S) are nothing but the total energies of the isolated T and S atoms. This quantity mainly reflects the intensity of the strong, intralayer Ti-S covalent bonds.

Note that the evaluation of the energetic quantities is given both considering the experimental configuration reported by Kasai *et al.* [66] (first and second column of Table 4), and employing the lattice constant c (third column of Table 4) obtained after longitudinal relaxation (fourth and fifth column of Table 4). We observe that quite

	CE (eV)	ILBE (meV/Å^2)	c (Å)	CE* (eV)	ILBE* (meV/Å^2)	V (Å^3)	q_A (e)	d(q_A) (eÅ)
rVV10	-15.602	-27.828	5.728	-15.603	-27.888	23.775	-0.860	0.380
rVV10(b=1.0)	-27.928	-192.073	4.934	-42.140	-1613.663	23.781	-0.861	0.383
rVV10(b=10.0)	-15.035	-16.609	5.878	-15.045	-17.698	23.574	-0.796	0.324
PBE	-15.150	-3.013	6.595	-15.189	-0.861	23.804	-0.871	0.404
LDA	-18.633	-17.275	5.470	-18.633	-18.357	23.648	0.829	0.383
rVV10*opt*	-25.889	-151.580	5.123	-25.310	-175.506	23.615	-0.809	0.373
Experiment	-14.805[83]		5.665[66]	-14.805		23.470[66]	-0.820[66]	0.030[66]
Theory (RPA)		-18.900[82]			-18.900	23.630[66]	-0.800[66]	0.340[66]
Theory (MBD)		-19.031			-19.031			

Table 4: Cohesive energy (CE) and interlayer binding energy (ILBE), see text for the definitions, obtained using the experimental lattice parameter c (first and second column) and the corresponding quantities (denoted by the * symbol, in the fourth and fifth column) relative to the c value (third column) optimized for each adopted functional. The reported reference CE and c values are experimental data, while, for the ILBE, we provide theoretical RPA[82] and MBD estimates. The quantity q_A, in the sixth column, represents the total charge belonging to the atomic basin A, surrounding the S atom. The charge q_A, contained in A, and the atomic dipole moment of the S atom, d(q_A), are reported in column seven and eight respectively.

similar results are achieved using PBE, rVV10, and rVV10(b=10.0), with an average discrepancy with the experimental reference value of ∼5 %. However, we point out that the CE value obtained with the rVV10(b=1.0) functional is largely overestimated. This turns out to be a clear effect of the artifical increasing of the strength of the short-range vdW interaction and reflects into a severe overbinding even of the Ti-S covalent bond. This is also confirmed by the analysis of the interlayer binding energy (ILBE), defined as $E(TiS_2) - E(TiS_2)_{c/a=5}$, representing the interaction energy between two adjacent layers of the material. Here, $E(TiS_2)_{c/a=5}$ indicates the total energy of the system when the c parameter is set to $5a \sim 17$ Å, which corresponds to a distance so large that the interlayer interaction is negligible. In order to have a more sound comparison with reference values, in addition to the RPA value reported in the literature[82], we have also computed the ILBE using the Many-Body Dispersion (MBD) approach[10] which allows for an effective RPA description of long-ranged vdW interactions, beyond conventional pairwise approximations.

The result achieved so far indicates overall correctness for the pseudopotential choice, and the general computational details employed. Further, they provide a starting point for a more detailed analysis regarding the electron density behavior, which will be presented in the next sections.

As already mentioned, Kasai *et al.*[66] pointed out that their DFT simulations were characterized by an interlayer S-S ED deformation significantly lower than the experimental one, implying that the X-ray diffraction data predict a stronger S-S interlayer interaction than DFT does. Moreover, since the experimental ED is characterized by 3 maxima in the direction of the 3 neighboring, symmetry-related S atoms, while the theoretical one exhibits only one maximum directed towards the center of the S-atom tetrahedron (see Figure 4), this suggests that the theoretical DFT description of the interlayer interactions indeed qualitatively differs from the experimental one. In order to investigate the reasons of this discrepancy, after setting up the TiS_2 bulk structure as reported in the experimental references [14], we carried out DFT calculation aimed to characterize in detail the electronic distribution in both intralayer and interlayer planes. In particular, there are three different interesting lines the main bonds of TiS_2 develop along:

- the intralayer Ti-S line
- the interlayer S-S line
- the interlayer S-center line

In particular, using the Bader nomenclature, for each line we characterize the (3, -3) critical point (CP) evaluating the position, $\mathbf{r}_{max}$, where the charge density reaches its maximum value, the density at this point, $n(\mathbf{r}_{max})$, and the Laplacian, $\nabla^2 n(\mathbf{r}_{max})$. It is worth to point out that the Laplacian of the electron density plays a crucial role in the qualitative description of this latter, since space points associated with positive Laplacian values are characterized by electronic depletion, while, viceversa, a negative Laplacian value corresponds to electronic accumulation.

3.1.2 Electron Density analysis of the intralayer plane

Firstly, we carry out the ED analysis along the Ti-S line of the intralayer plane, which leads to a detailed description of the strong, covalent bond, between the transition metal and the chalcogenide. The related results are presented, for all the functional schemes adopted, in Tab.5, while ED and respective Laplacian profiles are provided in Fig. 5. In this case we report only the PBE results, since no appreciable differences are observed for the other functionals. [14]

Two nonequivalent (3, −3) CPs are found along the Ti–S line. The (3, −1) CP is instead located at 1.12 Å from the Ti atom. As can be seen, looking at Table 5, very similar values are predicted by all the DFT functionals applied and most of these are also in good agreement with the experimental data.

(3, -3) CP #1	$\mathbf{r}_{max}$ (Å)	$n(\mathbf{r}_{max})$ (e/Å^3)	$\nabla^2 n(\mathbf{r}_{max})$ (e/Å^5)
rVV10	0.353	9.490	-253.367
rVV10(b=1.0)	0.350	9.487	-251.214
rVV10(b=10.0)	0.353	9.495	-252.613
PBE	0.352	9.497	-257.543
LDA	0.340	9.217	-221.444
rVV10*opt*	0.349	9.477	-255.304
Experiment[66]	0.407	9.350	-253.000
Theory[66] (SCAN+rVV10)	0.407	9.310	-250.000
(3, -3) CP #2	$\mathbf{r}_{max}$ (Å)	$n(\mathbf{r}_{max})$ (e/Å^3)	$\nabla^2 n(\mathbf{r}_{max})$ (e/Å^5)
rVV10	1.777	1.171	-10.315
rVV10(b=1.0)	1.782	1.175	-9.978
rVV10(b=10.0)	1.780	1.175	-10.789
PBE	1.781	1.172	-10.430
LDA	1.819	1.216	-10.091
rVV10*opt*	1.778	1.157	-10.165
Experiment[66]	1.714	1.260	-11.300
Theory[66](SCAN+rVV10)	1.707	1.200	-9.870
(3, -1) CP	$\mathbf{r}_{min}$ (Å)	$n(\mathbf{r}_{min})$ (e/Å^3)	$\nabla^2 n(\mathbf{r}_{min})$ (e/Å^5)
rVV10	1.122	0.453	1.455
rVV10(b=1.0)	1.126	0.448	1.211
rVV10(b=10.0)	1.122	0.450	1.484
PBE	1.120	0.458	1.231
LDA	1.125	0.461	1.002
rVV10*opt*	1.124	0.453	1.245
Experiment[66]		0.429	3.791
Theory[66] (SCAN+rVV10)		0.421	3.956

Table 5: Properties at the (3, -3) CPS and (3, -1) CP identified along the Ti-S line.

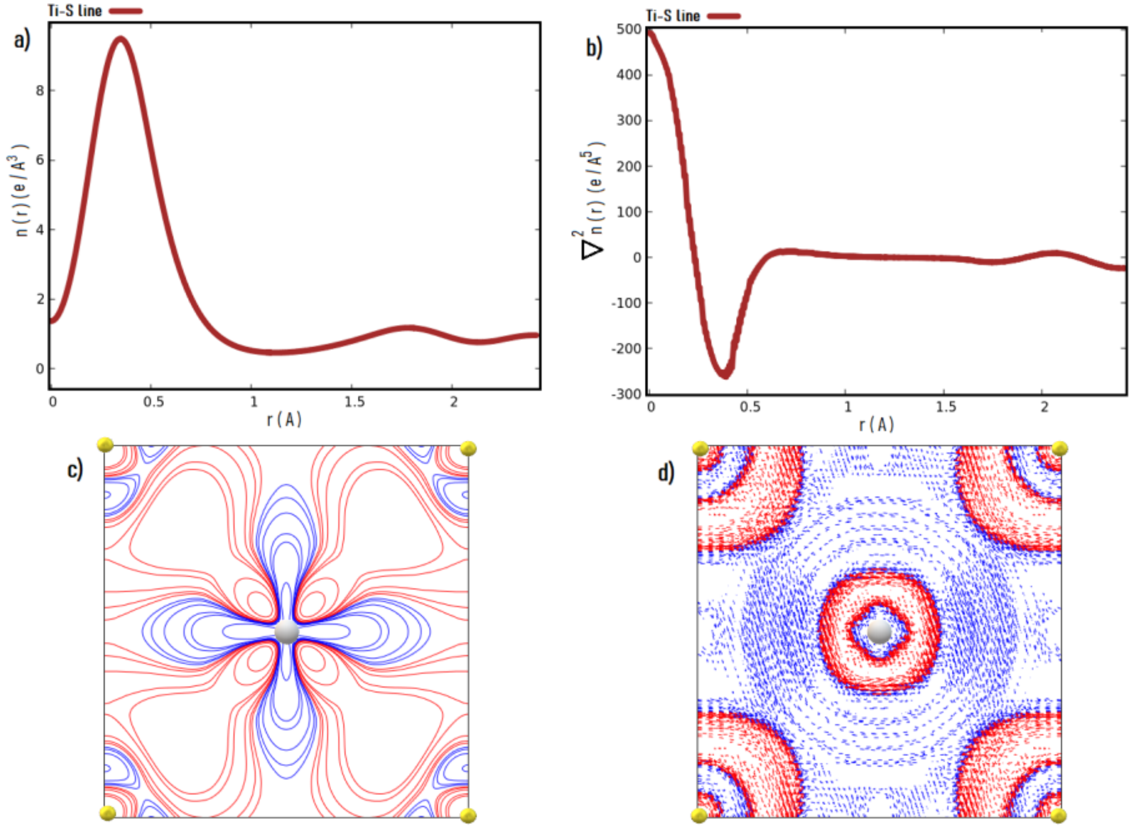

Figure 5: Ti-S intralayer bond. a) ED along the Ti-S line; local maxima denote the positions of the (3,-3) CPs, while the local minimum that of the (3,-1) one; b) Laplacian of the ED; c) ED deformation density map in the Ti-S plane; d) Laplacian map in the Ti-S plane. Here results obtained at the PBE level are reported as an example.

3.1.3 Electron Density analysis of the interlayer plane

A similar analysis is employed for the case of the interlayer plane as well. We consider the (3, -3) CP for both the S-S and S-center lines, and the (3, -1) CP along the the S-S line. The result achieved for all the functional schemes are summarized in Table 6 and 7, respectively.

In the interesting case of the S-S line, the PBE, rVV10, and rVV10(b=10.0) functionals predict a maximum value of the ED at a distance $\mathbf{r}_{max} \sim 0.61$ Å from the reference S atom, with a relative error of ~ 13 % with respect to the experimental result[66], while the error is slightly larger with rVV10(b=1.0) and LDA functionals.

	line	$\mathbf{r}_{max}$ (Å)	$n(\mathbf{r}_{max})$ (e/Å^3)	$\nabla^2 n(\mathbf{r}_{max})$ (e/Å^5)
rVV10	S - S	0.614	1.102	-9.163
	S - center	0.614	1.132	-10.052
rVV10(b=1.0)	S - S	0.607	1.050	-8.663
	S - center	0.605	1.081	-9.479
rVV10(b=10.0)	S - S	0.614	1.105	-9.222
	S - center	0.614	1.132	-9.985
PBE	S - S	0.614	1.095	-9.093
	S - center	0.614	1.129	-9.934
LDA	S - S	0.579	1.141	-10.016
	S - center	0.579	1.172	-11.419
rVV10*opt*	S - S	0.609	1.074	-8.950
	S - center	0.607	1.102	-9.766
Experiment[66]	S - S	0.707	1.150	-9.460
Theory[66](SCAN+rVV10)	S - center	0.711	1.080	-8.910

Table 6: Properties at the (3, -3) CP along the S-S and S-center lines, evaluated using different DFT functionals.

The $n(\mathbf{r}_{max})$ values are all very similar and in reasonable agreement with the experimental data, with the LDA functional that shows the best agreement with the experimental value. The rVV10(b=1.0) result, for which the maximum discrepancy occurs, has a deviation of only $\sim$ 9 %. The Laplacians values at the ED maximum point $\nabla^2 n(\mathbf{r}_{max})$, are also in acceptable agreement with the experimental values. Again, the result of the rVV10(b=1.0) functional exhibits the maximum deviation from the experiment, with a discrepancy of $\sim$ 8 %. This means that, at a distance r_{max} from the reference S atom, along the S-S line, with rVV10(b=1.0), the ED deformation is slightly smaller than for the other functionals.

For the S-center line a direct comparison with experimental data is not available, so we take as a reference the theoretical SCAN+rVV10 result reported by Kasai *et al.*[66]. The S-center line is characterized by the same $\mathbf{r}_{max}$ value found for the S-S line, again with a small deviation of the value obtained with rVV10(b=1.0) and LDA. Even in this case, the results for the ED and the Laplacians are in line with the theoretical reference

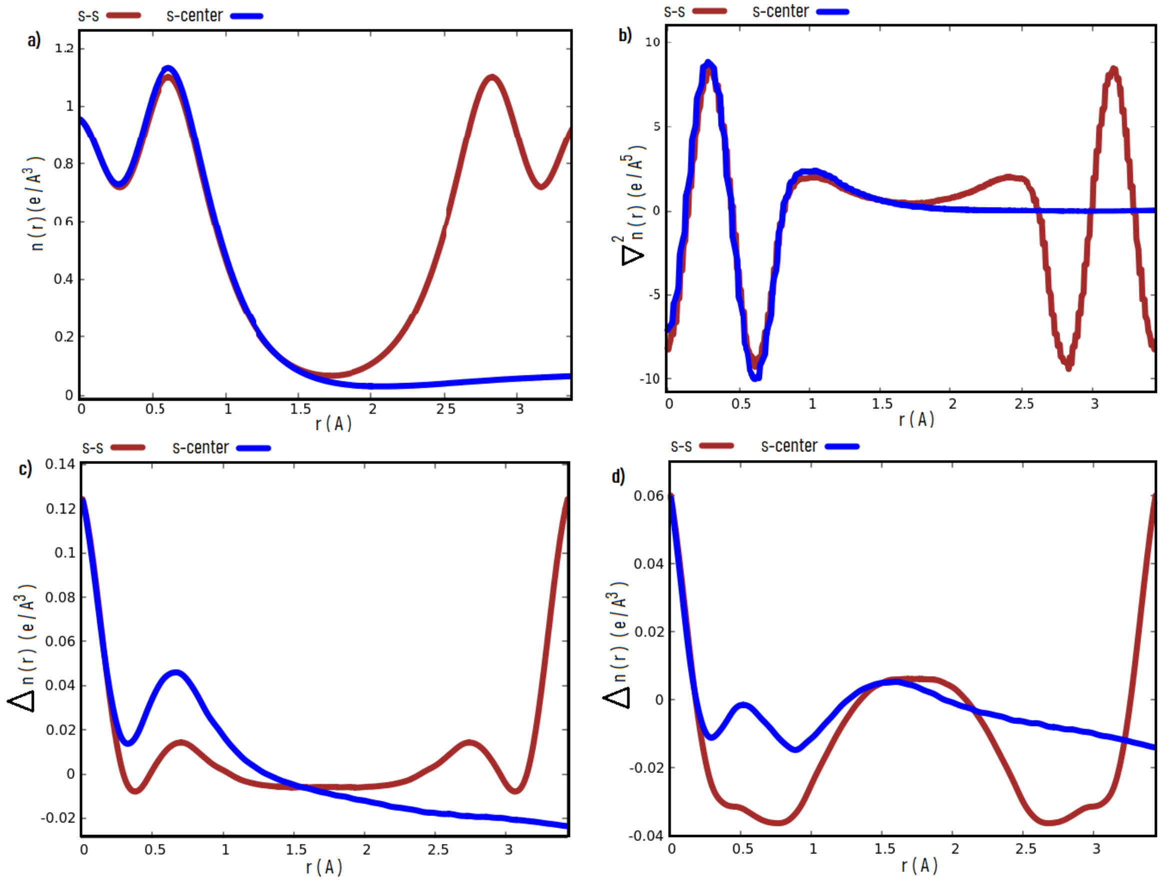

Figure 6: a) ED computed along the S-S and S-center line with the PBE functional. b) Corresponding Laplacian profiles. The small oscillations of the Laplacian profile are due to the finite-size of the real space mesh considered for the ED computation.In this case $\nabla^2 n(\mathbf{r}_{max})$ and $\nabla^2 n(\mathbf{r}_{min})$ are estimated by a parabolic interpolation $f(r \sim c) = c_2(r-c)^2 + k$, where the expansion center is $c = \mathbf{r}_{max}$ or $c = \mathbf{r}_{min}$. c) ED deformation Δ $n(\mathbf{r})$ computed using the PBE functional and d) the rVV10(b=1.0) functional. Curves obtained by rVV10 and rVV10(b=10.0) functionals are very similar to the PBE ones and therefore are not reported.

data.

Interestingly, for each functional employed, a slightly larger $n(\mathbf{r}_{max})$ value than that relative to the S-S line is observed, with a stronger ED deformation described by the associated Laplacian, indicating that the charge deformation along the S-center line is stronger than for the S-S line. The maximum deviation from the reference values, for both ED and Laplacians, occurs again for the LDA functional with an error of ∼ 8 % and ∼ 28%, respectively.

	$\mathbf{r}_{min}$ (Å)	$n(\mathbf{r}_{min})$ (e/Å^3)	$\nabla^2 n(\mathbf{r}_{min})$ (e/Å^5)
rVV10	1.718	0.068	0.486
rVV10(b=1.0)	1.718	0.079	0.461
rVV10(b=10.0)	1.718	0.067	0.481
PBE	1.718	0.067	0.460
LDA	1.718	0.070	0.468
rVV10*opt*	1.718	0.074	0.464
Theory[66](SCAN+rVV10)		0.058	0.727
Experiment[66]		0.086	0.691

Table 7: Properties at the (3, -1) CP along the S - S line, evaluated using different DFT functionals. The theoretical (SCAN+rVV10) result reported, is the result achieved after a multipolar refinement of the pure DFT density (see ref. [66] for details).

The S-S bond shows a symmetric ED distribution along the line connecting the two S atoms (see Figure 6a), with $\mathbf{r}_{min}$ exactly halfway between the two S atoms. Our computed $n(\mathbf{r}_{min})$ values, with the PBE, rVV10, and rVV10(b=10.0) functionals, as well as LDA, are in very good agreement with the DFT densities presented in ref. [66], exhibiting a significant underestimate (by about 22 %) of the ED at the interlayer BCP, with respect to the experimental value. Interestingly, using the rVV10(b=1.0) functional, the discrepancy with the experiment is instead considerably reduced to about 8 %. Note that the reported, theoretical SCAN+rVV10 value [66], is slightly below (and therefore slightly worse than) all our results.

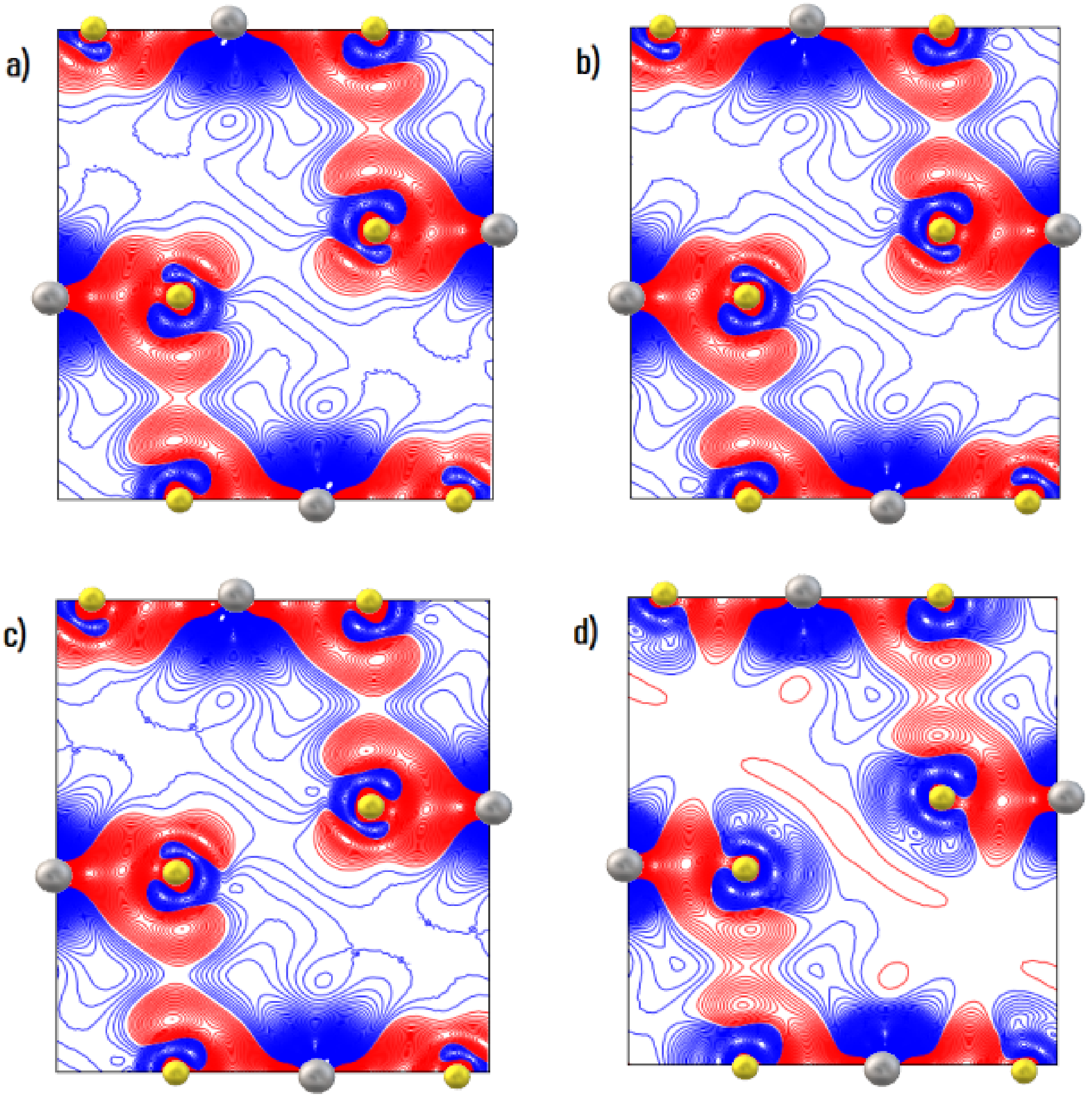

Figure 7: ED deformation map in the interlayer plane using four different functionals: a) PBE, b) rVV10, c) rVV10(b=10.0), and d) rVV10(b=1.0). The Ti atom are represented by grey spheres, while the S atoms are the yellow spheres. In the present maps, the smallest isoline value reported is 0.001 e/Å^3, with red and blue contours that represent charge accumulation and depletion, respectively. Note that the rVV10$_{\text{opt}}$ scheme results are not presented directly here, but they will be show separately at the end of this section.

For the (3, -1) CP, the Laplacian sign is always positive, as expected, indicating that the interlayer BCP located at $\mathbf{r}_{min}$ is a point where a charge depletion occurs. In Figure

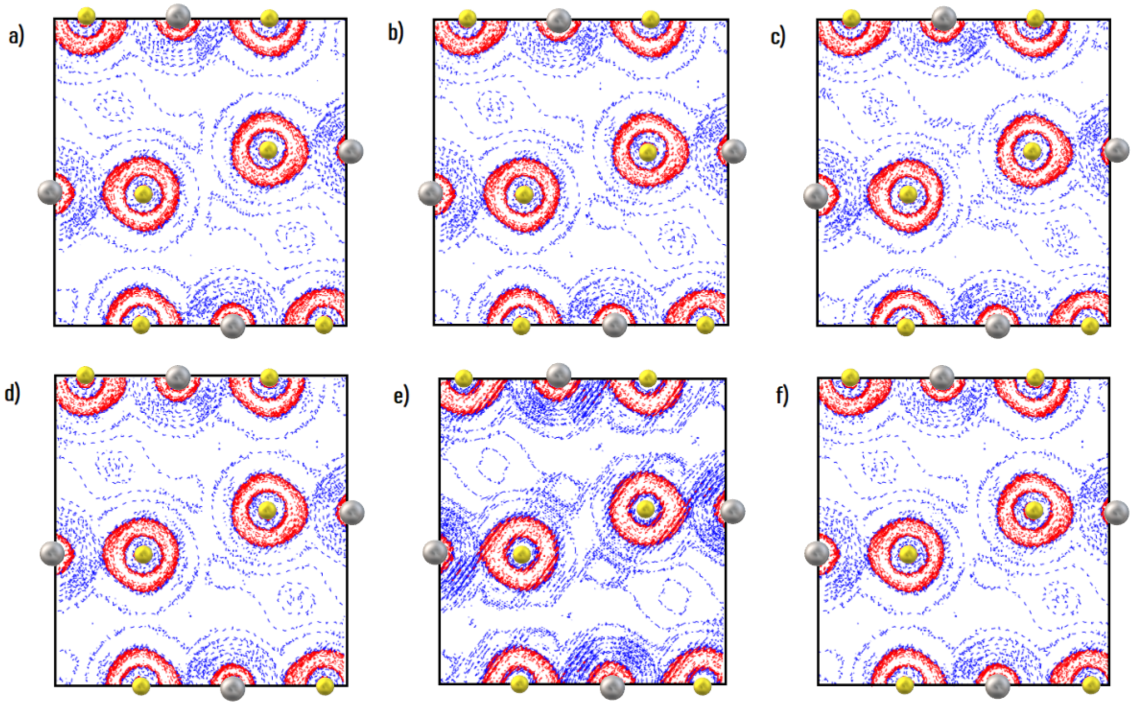

Figure 8: Laplacian map in the interlayer plane using different functionals: a) PBE, b) rVV10, c) rVV10(b=1.0), d) rVV10(b=10.0), e) rVV10*opt*, and f) rVV10*d*. The Ti atom are represented by grey spheres, while the S atoms are the yellow spheres. The results are reported by using Bader contour lines of [1, 2, 4, 8]× 10 $^{[-3,-2,-1,0,1]}$ e/Å^5. In these maps red (blue) contours are associated to negative (positive) laplacian values, which represents charge accumulation (depletion).

6a and 6b, an example of ED profiles and Laplacians, at the PBE level, along the S-S and S-center lines are shown, while in the bottom part, a comparison between the PBE ED deformation $\Delta n(\mathbf{r})$ (Figure 6c) and that obtained by rVV10(b=1.0) (Figure 6d) is made along the same lines, highlighting that rVV10(b=1.0) predicts a stronger charge depletion in the vicinity of the reference S atom than PBE and the other functionals. A consequent charge accumulation in the interlayer region appears, as confirmed by the higher ED $n(\mathbf{r}_{min})_{\mathrm{S-S}}$ at the (3, -1) CP accompanied by a smaller Laplacian value $\nabla^2 n(\mathbf{r}_{min})_{\mathrm{S-S}}$ (see Table 7) that indicates a slightly less charge depletion than for the other functionals considered.

The ED deformation map in the interlayer plane, presented in Figure 7, is very similar with the PBE, rVV10, and rVV10(b=10.0) functionals (as well as the LDA case which it is not reported), while the same is not true for rVV10(b=1.0), which predicts a more pronounced ED deformation in the region between the two S atoms belonging to adjacent layers. [14] The Laplacian map of the interlayer plane is presented in Figure 8: in this case, no significant differences for the functional schemes adopted up to now are found, as well as for LDA and the other schemes presented.

To overcome (at least partially) the evident shortcomings of both the artificially tuned rVV10(b=1.0) and rVV10(b=10.0) schemes, we try to modify the effect of the long range component of dispersion forces as well, which leads to the rVV10$_{\mathrm{opt}}$ density functional, already introduced at the beginning of this section. [14]

The ED deformation map obtained with this new functional is shown in Figure 9. As can be seen, by artificially manipulating the long-range component of vdW interactions, the unphysical ED accumulation in the intralayer S-S region seen for the rVV10(b=1.0) case disappears and, more interestingly, a small tendency to form a localized S-S interlayer bond can be observed, although the intensity of the interlayer ED deformation is again underestimated, being 7 times smaller than the experimental one[66]. The rVV10*opt* model preserves the nature of the S-Ti intralayer bond and the basic properties of the ED at the two non equivalent (3, -3) CPs and at the (3, -1) CP; in fact the positions of these points are unchanged and the ED and Laplacian values, reported in Table 6 and 7 respectively are in line with the other functionals employed. Similar conclusions hold considering the S-S and S-center lines. [14] Finally, one must point out that, even with this new functional, the ED accumulation along the S-S line is predicted to be smaller than along the S-center line, differently from the experimental findings. Also, considering the results presented in Table 4, rVV10*opt* still largely overestimates the ILBE, although it slightly reduces the dramatic overbinding of rVV10(b=1.0), one can conclude that it is not possible to achieve, at the same time, a description of energetic

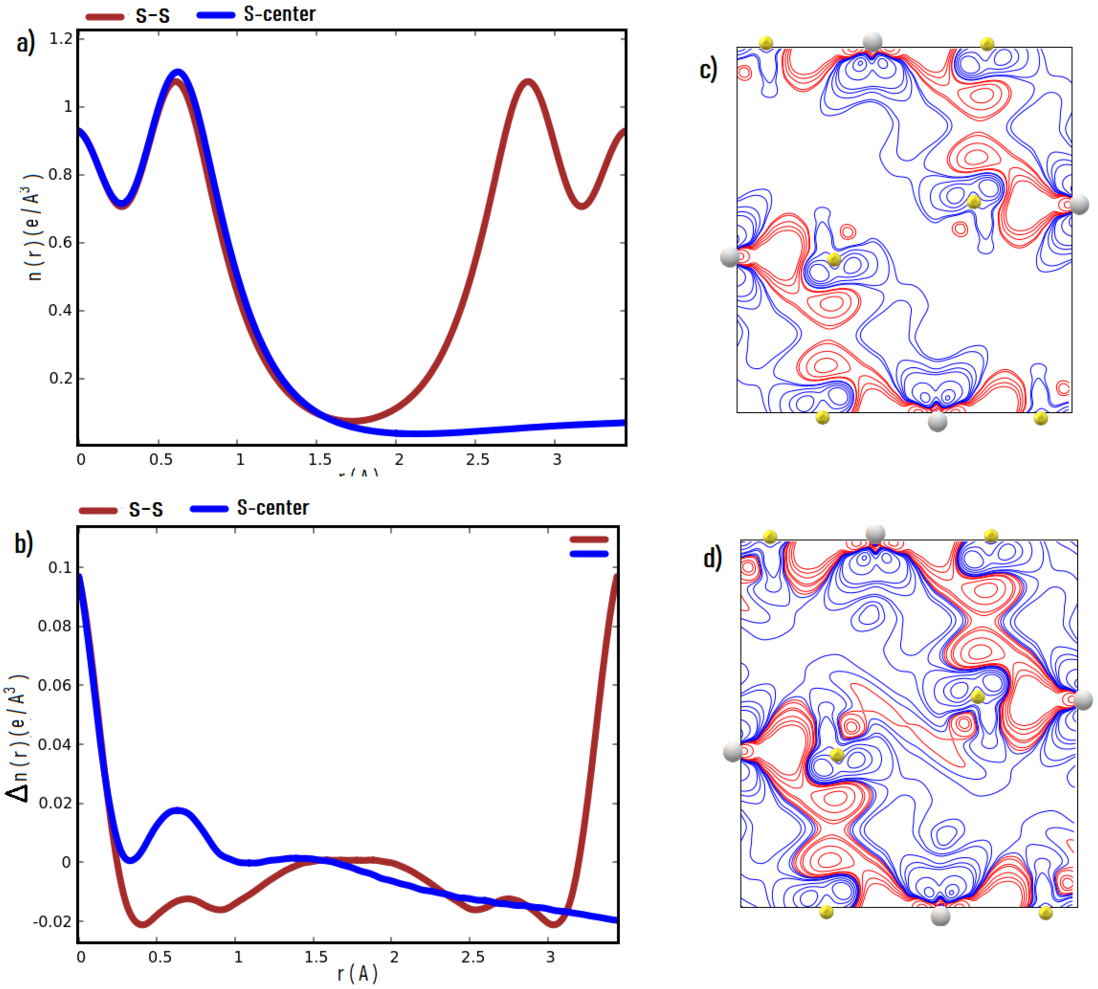

Figure 9: a) ED along the S-S and S-center line, obtained using the rVV10*opt* functional. b) Associated ED deformation $\Delta n(\mathbf{r})$. c) ED deformation map in the Ti-S intralayer plane. d) ED deformation map in the interlayer plane with a contour of ± 0.01 e/Å^3. e) ED deformation map in the interlayer plane with a smaller contour of ± 0.001 e/Å^3.

and ED deformation features, in reasonable agreement with the experimental results, by simply tuning the values of the b and C parameters of the rVV10 functional, which determine the strength of short/medium- and long-range vdW effects.

In the next section we adopt a different approach [14] to characterize the system of interest, employing a purposely generated, more flexible pseudopotential for the sulfur atom, which accounts for the d-electrons as well.

3.2 Application of Enhanced *d*-Orbitals Pseudopotential for the Sulfur Atom

As an alternative strategy to reduce the discrepancy between the theoretical DFT description of TiS_2 and the experimental evidence, we have also investigated the effect of introducing a modified pseudopotential for S. The S atom is characterized by the [Ne]$3s^2 3p^4$ ground-state configuration, so that in neutral S atom *d* orbitals are empty, and, in simple molecules, they are nearly unpopulated. Nonetheless, it was shown[80] that they can play a significant role: for instance, even in the small S_2 molecule an appreciable improvement in the binding-energy estimate was observed by adopting for S a pseudopotential built by taking into account *d* orbitals, which are expected[80] to give S enhanced polarizability and enable a great variety of bonding configurations through hybridization. In fact, although some orbitals (for instance, in this case the *d* ones) are not bound states of the neutral atom, it is necessary[80] [14] to choose a partially ionized atomic reference configuration, with a charge slightly different from the neutral atom, to get pseudopotentials that are better tailored for applications to solid-state and extended systems, since the effective configuration of these systems differs from that of the neutral atom.

	d (Å)	binding energy (eV)	vibrational frequency (cm^{-1})
rVV10	1.91	5.73	689
rVV10*d*	1.91	4.57	692
Experiment	1.89[80]	4.74[80]	714 ± 12[86]

Table 8: Equilibrium distance (d), binding energy, and vibrational frequency of the S_2 molecule, computed with the rVV10 and rVV10*d* functionals.

Following this interesting insight, we have generated a novel S ultra-soft pseudopotential, based on the configuration [Ne]$3s^2 3p^{3.0} 3d^{1.0}$, using the Troullier-Martins pseudization method[84] with non-linear core corrections.[85] Finally, we have coupled this pseudopotential with the rVV10 functional, developing in this way the rVV10*d* scheme.

In order to provide a grasp of the aforementioned evidence, we highlight the benefits induced by the major flexibility of our, novel *d*-orbitals-enhanced pseudopotential, by computing the equilibrium distance (*d*), the binding energy, and the vibrational frequency for another system: the S_2 molecule. Although its simplicity, the S_2 molecule certainly represents an interesting system to study, being an ubiquitous intermediate in the combustion, atmosphere, and interstellar space[86]. This preliminar analysis is carried out in the spirit of making a comparison between the rVV10 functional coupled with standard PAW and then with our novel pseudopotential (rVV10*d* method). The results are showed in Table 8 and comparison with experimental references clearly shows the importance of including *d* orbitals in such a system. In particular, considering the binding energy, the more than 20 % discrepancy with the experimental reference value of the rVV10 original functional, reduces to only about 3 % with rVV10*d*.

3.2.1 Application of the rVV10*d* method to TiS_2 and other Suflur-based TMDs

In this spirit, the energetic and electronic properties of TiS_2 has been recomputed using the new rVV10*d* functional. As can be seen in Table 9, at the (3, -3) and (3, -1) CPs, with rVV10*d*, the basic ED properties are very similar to those obtained by the standard rVV10 functional. [14]

However, the effect of replacing rVV10 with rVV10*d* gives surprisingly good effects looking at Figure 10 [14], which shows significant ED accumulation along the S-S line, leading to a description closer to the experimental one originally provided by Kasai *et al.*, which is not even present even with the SCAN+rVV10 adopted in the reference work[66]. The improvements observed are clearly due to the increased flexibility of the new S pseudopotentials that is able to better reproduce the variety of bonding structures and hybridization processes involving S atoms. Nevertheless, one has to point out that minor shortcomings are still present, since even with rVV10*d* the ED accumulation

(3, -3) CPs	line	$\mathbf{r}_{max}$ (Å)	$n(\mathbf{r}_{max})$ (e/Å^3)	$\nabla^2 n(\mathbf{r}_{max})$ (e/Å^5)
rVV10	S - S	0.614	1.102	-9.163
	S - center	0.614	1.132	-10.052
rVV10*d*	S - S	0.643	1.094	-9.253
	S - center	0.643	1.126	-9.990
Experiment[66]	S - S	0.707	1.150	-9.460
Theory[66](SCAN+rVV10)	S - center	0.711	1.080	-8.910

(3, -1) CP	line	$\mathbf{r}_{min}$ (Å)	$n(\mathbf{r}_{min})$ (e/Å^3)	$\nabla^2 n(\mathbf{r}_{min})$ (e/Å^5)
rVV10	S - S	1.718	0.068	0.486
rVV10*d*	S - S	1.718	0.068	0.482
Experiment[66]	S - S		0.086	0.691
Theory[66](SCAN+rVV10)	S - S		0.058	0.727

Table 9: Properties at the (3, -3) CPs along both the S-S and S-center line and at the (3, -1) CP on the S-S line, computed using rVV10*d* and compared with the results achieved with rVV10.

along the S-S line is predicted to be slightly smaller than along the S-center line.

We proceed by recomputing the structural and energetical quantities presented so far, together with the atomic basin volume, the charge contained within it and the S atom dipole moment. As can be seen in Table 11, the good energetic description of rVV10*d* is preserved even considering a TiS_2 configuration where the experimental lattice constant c is replaced by the c value optimized with rVV10*d* (whose prediction is only slightly worse than the rVV10 one), thus increasing the confidence in the reliability of this functional. Remarkably, with rVV10*d*, an even more substantial improvement in energetic properties takes place. In fact, while the CE remains very close to that obtained by rVV10, suggesting that *d* orbitals of S do not play a significant role in the formation of strong, intralayer covalent bonds, the change in the ILBE is instead considerable: assuming the experimental structure, our computed ILBE differs by only ~ 2 meV/Å^2 from the theoretical references, i.e. high quality, RPA,[82] and MBD estimates, which represents a relative error of about 10 %; such an error is comparable to that obtained

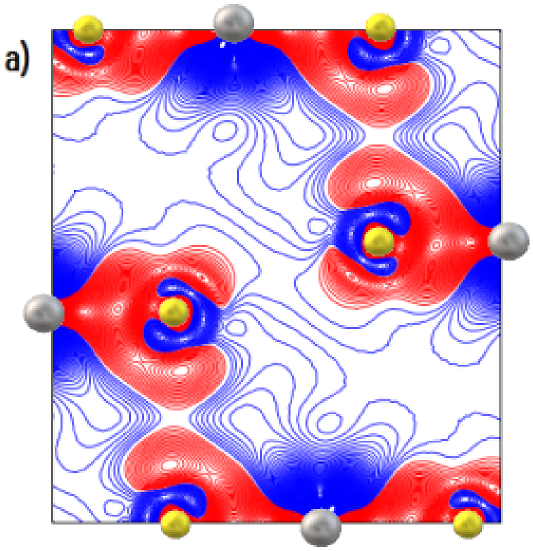

Figure 10: Comparison between the ED deformation obtained by the standard rVV10 functional (panel a) and rVV10*d* (panel b). The smallest isoline value reported is 0.001 e/Å^3, with red and blue contours that represent charge accumulation and depletion, respectively.

by the much more expensive meta-GGA approaches and is much smaller than that (about 47 %) found with the original rVV10 functional which clearly overbinds [14].

	rVV10*d*			rVV10		
	ILBE (meV/Å^2)	c (Å)	ILBE* (meV/Å^2)	ILBE (meV/Å^2)	c (Å)	ILBE* (meV/Å^2)
TiS_2	-20.771	5.809	-20.888	-27.828	5.728	-27.888
ref.[82]	-18.900	5.665	-18.900	-18.900	5.665	-18.900
MoS_2	-20.296	12.810	-22.147	-29.242	12.530	-29.683
ref.[82]	-20.530	12.300	-20.530	-20.530	12.300	-20.530
TaS_2	-18.924	6.152	-19.344	-29.367	6.009	-29.369
ref.[82]	-17.680	5.900	-17.680	-17.680	5.900	-17.680
HfS_2	-18.391	5.938	-18.530	-23.452	5.858	-23.603
ref.[82]	-16.130	5.840	-16.130	-16.130	5.840	-16.130
ME	-1.285	0.251	-1.917	-9.162	0.105	-9.362
MARE (%)	7.5	3.2	10.7	50.3	1.3	51.1

Table 10: Optimized lattice constant c, ILBE and ILBE* computed for TiS_2 and three other TMDs, employing both rVV10 and rVV10*d* functionals. The last two lines report the mean error(ME) and the mean absolute relative error (MARE).

As far as the dipole moment is concerned, with rVV10*d* this quantity is not improved with respect to the experimental estimate (see Table 11), which can be rationalized as follows: as a consequence of applying the modified rVV10*d* functional, the electronic charge is more widespread around the S atoms, which leads to a better agreement with experimental ED findings and to an improved estimate of the ILBE. However this increased charge delocalization does not occur exclusively in the interlayer region, but also, for instance, in the intralayer region, particularly along lines connecting neighboring S atoms. Therefore, the net delocalization effect (see Figure 10) is approximately isotropic so that the S dipole moment is not appreciably changed from that estimated by the original rVV10 functional. [14]

	CE (eV)	ILBE (meV/Å^2)	c (Å)	CE* (eV)	ILBE* (meV/Å^2)	V (Å^3)	q$_A$ (e)	d(q$_A$) (eÅ)
rVV10	-15.602	-27.828	5.728	-15.603	-27.888	23.775	-0.860	0.380
rVV10*d*	-15.640	-20.888	5.809	-15.646	-20.771	23.761	-0.860	0.390
Experiment	-14.805[83]		5.665[66]	-14.805		23.470[66]	-0.820[66]	0.030[66]
Theory (RPA)		-18.900[82]			-18.900	23.630[66]	-0.800[66]	0.340[66]
Theory (MBD)		-19.031			-19.031			

Table 11: Energetic and structural properties of TiS$_2$, together with the atomic basin properties of the S atom, obtained with rVV10*d* and compared with rVV10. The notation used is the same as in Table 4.

To further assess the validity of this novel approach, we have applied the rVV10*d* functional to other three different TMDs, whose chalcogen is always the S atom: MoS$_2$, TaS$_2$, and HfS$_2$. The results for the equilibrium lattice parameter c, as well as the ILBE and ILBE* (see Table 10), are very promising. [14] The major flexibility of the new pseudopotential, embedded in rVV10*d* scheme, dramatically improves the energetic description of S-based TMDs, maintaining an appreciable quality of the estimate of the longitudinal lattice parameter c: in fact, although the error relative to c is ~ 2 % bigger than with rVV10, the mean absolute relative error (MARE) of the ILBE is reduced by about *five* times; this means that the pronounced overbinding tendency of rVV10 is almost totally eliminated. [14]

4 Conclusions

We have investigated vdW interactions from both fundamental, theoretical perspective [13], and computational as well [14], particularly focusing on the improvement of the description of vdW effects in the framework of DFT. Exploring a wide range of physical interesting scenarios, we overcame mathematical challenges, achieving a promising theoretical method based on a sum-rule approach [13], and, making use of physical insights, we understood the importance of d electrons in S atom, almost totally closing the gap between theory and experiment for the puzzling case of TiS_2 [14].

For what concerns the first section of this Thesis, we developed an exact, comprehensive theory for the ground state static polarizability α_0 and the long-range vdW energy functional, demonstrating the application to simple, interesting physical systems [13]. Our approach uses a sum-rule and takes only monomer ground-state properties as input. The functionals are evaluated via solution of a single position-space differential equation, without the usual explicit excited-state summations or frequency integrations [13]. A comparison to results obtained with the VV09 functional shows good agreement with our exact results for H but not for the QHO or SW systems. This supports the general notion that non-local energy functionals in the LL/VV class can perform well in the real chemical systems for which they were designed but can fail for idealized models, where the tails of the ground-state densities decay very differently from those typically encountered in chemistry. As a result of its general mathematical foundation, the present theory has general validity and could be applied to many electron systems and extended to higher multipoles [13]. Generalization to hydrogenic atom with nuclear charge Z and excited state polarizabilities for the system considered are straightforward, while further, more challenging developments can be carried on. For example, for what concerns still simple, real atomic systems, one could consider the He atom, approximating the ground state wavefunction as a Slater determinant, while, for alkali atoms, such as Li, Na, K, Rb, Cs, Fr, an interesting approach could be that of modeling the core electrons as a whole, computing the ground state electron density by means of already existing density functional theories, and adopting our sum-rule approach for the valence electron.

In the second section we presented the results of a first-principles, DFT investigation, of the energetic and electronic properties of TiS_2 [14], a system where a puzzling discrepancy, between the distribution of the electron density obtained by X-ray diffraction data and that computed by state-of-the DFT schemes has been reported. In particular this disagreement arises in the interlayer region, between S atoms belonging to adjacent layers. We studied the system employing several DFT schemes, achieving a theoretical description very close to the one already reported in the literature [66], thus, reflecting the same shortcomings already pointed out [14]. One should emphasize that this is true for both local and non-local functional schemes. In fact, although non local density functionals better perform than local ones, nevertheless, we clearly show that even the formers are unable -exactly as their local counterpart- to proper describe some of the trickiest features of TiS_2. In attempting to improve the DFT description, we then focused on artificially tuning the intensity of both short/medium and short-range vdW interaction, founding that the significant charge accumulation in the interlayer region between two S atoms predicted, for instance, by rVV10($b = 1.0$), comes at the expenses of an unphysical increasing of the interlayer binding energy and of the cohesion energy as well [14], again confirming that neither the non-locality, nor the simple tuning of vdW interactions intensity was the key to overcome the discrepancy. In this case, actually, the specific adopted functional seems to play a less crucial role than the chosen pseudopotential. In fact, the real improvement of the description is observed by adopting a *d*-electron enhanced pseudopotential for the S atom, since, as pointed out by previous works as well, it has been demonstrated that the *d* level, not relevant when the S atom is isolated, plays a fundamental role when this latter has a tendency to create chemical bonding with the surrounding atoms, such as in the case of TiS_2. Adopting the purposely generated, novel pseudopotential with rVV10 method (rVV10*d* scheme), leads to significant improvements not only concerning the interlayer electron density map, but also correcting the well-known tendency of non-local density functional to overestimate the interlayer binding energy in vdW materials [82]. Even within our rVV10*d* scheme, a residual discrepancy with the experiment regarding the position of the electron density maxima and the atomic dipole moment of the S atom is still present. [14] Probably, this could be eliminated only by an higher-level theoretical, first-principles approach, such as a quantum Monte Carlo scheme, able to include the whole set of correlation effects. Such an approach, however, would be extremely expensive computationally because very small ED deformations could only be accurately reproduced by very long simulations to get a sufficiently small statistical error associated with differential densities. In any case, although all fine details in the ED deformation map cannot be captured by rVV10*d*, nonetheless we suggest that this DFT functional indeed represents a reasonable compromise between accuracy and efficiency for improving the theoretical description of TiS_2. Additional investigations indicate that similar improvements, particularly in the evaluation of energetic terms, can be obtained by DFT calculations based on the $rVV10_d$ functional, applied also to other TMD materials containing S atoms and characterized by the same structure of TiS_2, such as TaS_2, HfS_2, and MoS_2 [14].

5 Appendix

5.1 VV09 Density Functional

VV09 [62] is a nonlocal van der Waals density functional introduce in 2010 by Vydrov and Van Voorhis, as an improved version of its predecessor vdW-DF-04. The total correlation energy of VV09 has the following analytical form $E_c = E_c^{\text{nl}}$, where the nonlocal component of the correlation energy can be expressed as follow:

$$E_c^{\text{nl}} = \frac{1}{2}\int d\mathbf{r}\,\frac{n(\mathbf{r})}{\omega_0(\mathbf{r})}\int d\mathbf{r'}\,\frac{n(\mathbf{r'})}{\omega_0(\mathbf{r'})}\frac{\mathrm{D(K)\,Q^6}}{\omega_0(\mathbf{r})+\omega_0(\mathbf{r'})}$$

where $n(\mathbf{r})$ is the ground state electron density of the system and ω_0 can be written as $\omega_0 = \sqrt{\omega_p^2/(3+\omega_g^2)}$, which depends respectively on the plasma frequency and the local band gap as:

$$\begin{cases} \omega_p(\mathbf{r}) = 4\pi n(\mathbf{r}) \\ \omega_g(\mathbf{r}) = 0.0089\,|\nabla n(\mathbf{r})/n(\mathbf{r})|^4 \end{cases} .$$

Further, defining $K = |\mathbf{r}-\mathbf{r'}|\,Q(\mathbf{r}-\mathbf{r'})$, one has

$$Q = \frac{1}{2}\left[\frac{k(\mathbf{r})\,k(\mathbf{r'})}{k(\mathbf{r})+k(\mathbf{r'})}\right]^{1/2}$$

k can be again expressed in term of the electron density as $k(\mathbf{r}) = 4(3n(\mathbf{r})/\pi)^{1/3}\phi^2$. Where ϕ is the spin-scaling factor

$$\phi(\zeta) = \frac{(1+\zeta)^{2/3}+(1-\zeta)^{2/3}}{2}$$

and ζ is the relative spin polarization $\zeta = (n_\alpha - n_\beta)/(n_\alpha + n_\beta)$. Finally the function D(K) ha the form:

$$D(K) = B\left(2A - \frac{3}{2}B\right)$$

and

$$\begin{cases} A = \frac{2}{\sqrt{\pi}}e^{-K^2} \\ B = \frac{\text{erf(K)}}{K^3} - \frac{A}{K^2} \end{cases} .$$

The nonlocal van der Waals functional VV09 has been implemented self-consistently and benchmarked in comparison with vdW-DF-04 on the popular S22 test set of weakly bound complexes, finding that the VV09 correlation energy model performs reasonably well with HF exchange.

The VV09 framework has brought improvements on the formulation of the dispersion energy as well. This was done introducing the Clausius-Mossotti formula (which relates the polarizability to the electric permittivity of the medium) in the previous forumlation made by Andersson, Langreth and Lundqvist (ALL) theory [18]. This leads to the following expression for the dynamic polarizability

$$\alpha(\mathbf{r}, iu) = \frac{1}{4\pi}\frac{\omega_p^2(\mathbf{r})}{\omega_p^2(\mathbf{r})/3 + \omega_g(\mathbf{r}) + u^2}$$

The long-range dispersion interaction energy between systems A and B can then be written [61] in terms of local polarizabilities as:

$$E_{\text{disp}} = \frac{3}{\pi}\int_0^\infty du \int_A d\mathbf{r} \int_B d\mathbf{r'} \frac{\alpha(\mathbf{r}, iu)\alpha(\mathbf{r'}, iu)}{|\mathbf{r} - \mathbf{r'}|^6}$$

which within the VV09 frameworks reads as

$$E_{\text{disp}} = -\frac{3}{32\pi^2}\int_A d\mathbf{r}\int_B d\mathbf{r'}\frac{\omega_p(\mathbf{r})^2\omega_p(\mathbf{r'})^2|\mathbf{r}-\mathbf{r'}|^{-6}}{\omega_0(\mathbf{r})\omega_0(\mathbf{r'})[\omega_0(\mathbf{r})+\omega_0(\mathbf{r'})]} \tag{56}$$

where the integration on the imaginary frequencies has been carried out.

5.2 rVV10 Density Functional

rVV10 [12] certainly represents one of the best vdW-corrected functionals nowadays available; it takes into account the entire range of vdW interactions at a reasonable computational cost using only the ED $n(\mathbf{r})$ as input. In particular, the rVV10 non-local correlation energy has the following expression:

$$E_c^{NL} = \int\int n(\mathbf{r})\phi_{\text{rVV10}}(\mathbf{r}\,,\mathbf{r'})n(\mathbf{r'}) \tag{57}$$

where ϕ_{rVV10} is the non-local correlation kernel, which is:

$$\phi_{\text{rVV10}} = -\frac{3e^4}{2m^2}\frac{1}{(q(\mathbf{r})R^2+1)(q(\mathbf{r'})R^2+1)[(q(\mathbf{r})\ +\ q(\mathbf{r'}))R^2+2]} \tag{58}$$

In the above expression $R = |\mathbf{r}-\mathbf{r'}|$ and $q(\mathbf{r})$ is a function of the ED and its gradient:

$$q(\mathbf{r}) = \frac{\omega_0(n(\mathbf{r}),\nabla n(\mathbf{r}))}{k(n(\mathbf{r}))} \tag{59}$$

where

$$\omega_0 = \sqrt{C\frac{\hbar^2}{m^2}\left|\frac{\nabla n(\mathbf{r})}{n(\mathbf{r})}\right|^4+\frac{1}{3}\frac{4\pi n(\mathbf{r})e^2}{m}} \tag{60}$$

and

$$k(n(\mathbf{r})) = 3\pi b\left(\frac{n(\mathbf{r})}{9\pi}\right)^{1/6}\ . \tag{61}$$

The total XC functional is then obtained by adding the non-local correlation energy to the refitted Perdew-Wang exchange functional[69] and the Perdew-Wang LDA correlation[71] functional, as proposed in the seminal work by Vydrov and Van Voorhis:[68]

$$E_{xc}^{NL} = E_x^{rPW86} + E_c^{LDA} + E_c^{NL} \ . \tag{62}$$

The rPW86 exchange functional was chosen mainly because it is nearly vdW-free,[69] in such a way to avoid double-counting effects. In eq. (60) the C parameter represents the so-called local band gap and is tuned to give accurate asymptotic vdW C_6 coefficients, thus regulating the behavior of the long-range component of vdW interactions. The fitting procedure, aimed to minimize the average error for a benchmark set of 54 C_6 coefficients, was originally carried out by Vydrov and Van Voorhis,[68] leading to an optimal value of $C = 0.0093$. Another essential aspect of the VV10 (and its successor rVV10) formalism is the presence of a second adjustable parameter, b (see eq. (61)),which controls the short range behavior of the non-local correlation energy. This means that when E_c^{NL} is added to the other energetic terms, the b parameter is adjusted to merge the interaction energy contributions at short and intermediate ranges. With an empirical fitting procedure on the S22 binding-energy data set,[70] Vydrov and Van Voorhis proposed a value of $b = 5.9$.[68] After the implementation of the efficient Roman-Perez, Soler[72] interpolation scheme in the reciprocal space, this value was revised by Sabatini and coworkers to $b = 6.3$.[12]

We have chosen rVV10 as the basic DFT functional to investigate the effect of vdW interactions in the ED distribution of TiS_2 also because of the possibility to separately modify the intensity of both short- and long-range vdW interactions in a transparent way by simply tuning the two adjustable parameters b and C mentioned above. First the short-range component is analyzed. This is done by considering two different regimes: the former in which the value of the b parameter is increased to b=10.0, thus damping the intensity of short range vdW interactions, and the latter in which b is reduced to b=1.0, that instead results in a substantial increase of the intensity of the short-range vdW interaction.

6 References

References

[1] Van der Waals J.D., Over de Continuiteit van den Gas- en Vloeistoftoestand (on the continuity of the gas and liquid state), *PhD thesis*, **1873**.

[2] W. Kohn and D. E. Makarov, *Phys. Rev. Lett.*, **1998**, *80*, 4153.

[3] R. Eisenhitz and F. London, *Z. Phys.*, **1930**, *60*, 491.

[4] Grimme S. , Semiempirical GGA-type density functional constructed with a long-range dispersion correction, *J. Comp. Chem*, **2006)** , *27*, 1787.

[5] N. Marzari and D. Vanderbilt, *Phys. Rev. B*, **1997**, *56*, 1284.

[6] P. L. Silvestrelli, *Phys. Rev. Lett.*, **2008**, *100*, 053002.

[7] P. L. Silvestrelli, A. Ambrosetti, *Phys. Rev. B*, **2013**, *87*, 075401.

[8] P. L. Silvestrelli, *J. Chem. Phys.*, **2013**, *139*, 054106 .

[9] P. L. Silvestrelli, K. Benyahia, S. Grubisic, F. Ancilotto, and F. Toigo, *J. Chem. Phys.*, **2009**, *130*, 074702.

[10] Tkatchenko A., DiStasio Jr. R.A., Car R., Scheffler M. Accurate and Efficient Method for Many-Body van der Waals Interactions *Phys. Rev. Lett.*, **2012**, *108*, 236402.

[11] Vydrov O.A., Van Voorhis T., Dispersion Interactions From a Local Polarizability Model. *Phys. Rev. A*, **2010**, *81*, 062708.

[12] Sabatini R.; Gorni, T.; de Gironcoli, S. Nonlocal van der Waals density functional made simple and efficient. *Phys. Rev. B* **2013**, *87*, 041108.

[13] M. Ricci, P. L. Silvestrelli, J. F. Dobson, A. Ambrosetti, Exact Sum-Rule Approach to Polarizability and Asymptotic van der Waals Functionals Derivation of Exact Single-Particle Benchmarks *J. Phys. Chem. Letters*, **2022**, *13*, 8298.

[14] M. Ricci, A. Ambrosetti, P. L. Silvestrelli, Improving the Description of Interlayer Bonding in TiS2 by Density Functional Theory *J. Phys. Chem C*, **2020**, *124*, 27592.

[15] Dalgarno a., Lewis J.T. The Exact Calculation of Long-Range Forces Betweeen Atoms by Perturbation Theory. *Proc. R. Soc. London, Ser. A*, **1955**, *233*, 70-74.

[16] Burke K. Perspective on Density Functional Theory. *J. Chem. Phys.*, **2012**, *136*, 150901.

[17] Perdew J.P., Burke K., Ernzerhof M. Generalized Gradient Approximation Made Simple *Phys. Rev. Lett.*, **1996**, *77*, 3865.

[18] Y. Andersson, Langreth D. C., Lundqvist B. I. Van der Waals Interactions in Density-Functional Theory. *Phys. Rev. Lett.*, **1996**, *76*.

[19] Dion M., Rydberg H., Schröder E., Langreth D. C., Lundqvist B. I. Van der Waals Density Functional for General Geometries. *Phys. Rev. Lett.*, **2004**, *92*, 246401.

[20] Peng H., Yang Z.-H., Perdew J. P., Sun J. Versatile van der Waals Density Functional Based on a Meta-Generalized Gradient Approximation. *Phys. Rev. X*, **2016**, *6*, 041005.

[21] Ambrosetti A., Silvestrelli P.L. Adsorption of Rare-Gas Atoms and Water on Graphite and Graphene by van der Waals-Corrected Density Functional Theory. *J. Phys. Chem. C*, **2011**, *115*, 3695-3702.

[22] Grimme,S. Semiempirical GGA-Type Density Functional Constructed with a Long-Range Dispersion Correction. *Comp. Chem.*, **2006**, *27*, 1787-1799.

[23] Johnson E.R., Becke A.D. Van der Waals Interactions from the Exchange Hole Dipole Moment: Application to Bio-Organic Benchmark Systems. *Chem. Phys. Lett.*, **2006**, *432*, 600-603.

[24] Silvestrelli P.L. Van der Waals Interactions in DFT Made Easy by Wannier Functions. *Phys. Rev. Lett.*, **2008**, *100*, 053002.

[25] Ambrosetti A., Silvestrelli P.L. van der Waals Interactions in Density Functional Theory Using Wannier Functions: Improved C6 and C3 Coefficients by a Different Approach. *Phys. Rev. B*, **2012**, *85*, 073101.

[26] Tkatchenko A., Scheffler M. Accurate Molecular van der Waals Interactions from Ground-State Electron Density and Free-Atom Reference Data. *Phys. Rev. Lett.*,**2009**, *102*, 073005.

[27] Ambrosetti A., Reilly A.M., DiStasio Jr. R.A., Tkatchenko A. Long-Range Correlation Energy Calculated from Coupled Atomic Response Functions. *J. Chem. Phys.*, **2014**, *140*, 18A508.

[28] Steinmann S. N., Corminboeuf C. A Generalized-Gradient Approximation Exchange Hole Model for Dispersion Coefficients. *J. Chem. Phys.*, **2011**, *134*, 044117.

[29] Hauseux P., Nguyen T.T., Ambrosetti A., Ruiz K.S., Bordas S., Tkatchenko A. From Quantum to Continuum Mechanics in the Delamination of Atomically-Thin Layers from Substrates. *Nat. Commun.*, **2020**, *11*, 1-8.

[30] Hauseux P., Ambrosetti A., Bordas S., Tkatchenko A. Colossal Enhancement of Atomic Force Response in van der Waals Materials Arising from Many-Body Electronic Correlations. *Phys. Rev. Lett.*, **2022**, *128*, 106101.

[31] Agnoli S., *et al.* Unraveling the Structural and Electronic Properties at the WSe2–Graphene Interface for a Rational Design of van der Waals Heterostructures. *ACS Appl. Nano Mat.*, **2018**, *1*, 1131-1140.

[32] Graziano G., Klimes J., Fernandez-Alonso F., Michaelides A. Improved Description of Soft Layered Materials with van der Waals Density Functional Theory *J. Phys. Cond. Matt.*, **2012**, *24*, 424216.

[33] Ambrosetti A., Alfé D., DiStasio Jr. R.A., Tkatchenko A. Hard Numbers for Large Molecules: Toward Exact Energetics for Supramolecular Systems. *J. Phys. Chem. Lett.*, **2014**, *5*, 849-855.

[34] Grimme S. Supramolecular Binding Thermodynamics by Dispersion-Corrected Density Functional Theory *Chem.-A Eur. J.*, **2012**, *18*, 9955-9964.

[35] Whittleton S.R., Otero-De-La-Roza A., Johnson E.R. Exchange-Hole Dipole Dispersion Model for Accurate Energy Ranking in Molecular Crystal Structure Prediction. *Angew. Chem. Intl. Ed.*, **2014**, *53*, 7879-7882.

[36] Reilly A.M., Tkatchenko A. Understanding the Role of Vibrations, Exact Exchange, and Many-Body van der Waals Interactions in the Cohesive Properties of Molecular Crystals. *J. Chem. Phys.*, **2013**, *139*, 024705.

[37] Tkatchenko A., Rossi M., Blum V., Ireta J., Scheffler M. Unraveling the Stability of Polypeptide Helices: Critical Role of van der Waals Interactions. *Phys. Rev. Lett.*, **2011**, *106*, 118102.

[38] Ferri N., DiStasio Jr. R.A., Ambrosetti A., Car R., Tkatchenko A. Electronic Properties of Molecules and Surfaces with a Self-Consistent Interatomic van der Waals Density Functional. *Phys. Rev. Lett.*, **2015**, *114*, 176802.

[39] Thonhauser T., *et al.* Van der Waals Density Functional: Self-Consistent Potential and the Nature of the van der Waals Bond. *Phys. Rev. B*, **2007**, *76*, 125112.

[40] Vydrov O.A., Van Voorhis T. Improving the Accuracy of the Nonlocal van der Waals Density Functional with Minimal Empiricism. *J. Chem. Phys.*, **2009**, *130*, 104105.

[41] Kooi D.P., Gori-Giorgi P. A Variational Approach to London Dispersion Interactions Without Density Distortion. *J. Phys. Chem. Lett.*, **2019**, *10*, 1537-1541.

[42] Hyldgaard P., Jiao Y., Shukla V. Screening Nature of the van der Waals Density Functional Method: a Review and Analysis of the Many-Body Physics Foundation. *J. Phys.: Condens. Matter*, **2020**, *32*, 393001.

[43] Gould T. How Polarizabilities and C_6 Coefficients Actually Scale with Volume. *J. Chem. Phys.*, **2016**, *145*, 084308.

[44] Szabó P., Góger S., Charry J., Karimpour M.R., Fedorov D.V. , Tkatchenko A. Four-Dimensional Scaling of Dipole Polarizability in Quantum Systems. *Phys. Rev. Lett.*, **2022**, *128*, 070602.

[45] Resta R. Macroscopic Polarization in Crystalline Dielectrics: the Geometric Phase Approach. *Rev. Mod. Phys.*, **1994**, *66*, 899.

[46] Gould T., Bucko T. C6 Coefficients and Dipole Polarizabilities for All Atoms and Many Ions in Rows 1–6 of the Periodic Table. *J. Chem. Th. Comput.*, **2016**, *12*, 3603–3613.

[47] Choy T.C. van der Waals Interactions of the Hydrogen Molecule: an Exact Implicit Density Functional. *Phys. Rev. B*, **2000**, *26*, 012506.

[48] Ambrosetti A., *et al.*, Wavelike Charge Density Fluctuations and van der Waals Interactions at the Nanoscale, *Science*, **2016**, *351*, 1171-1176.

[49] Colossal Enhancement of Atomic Force Response in van der Waals Materials Arising from Many-Body Electronic Correlations. Hauseux P., Ambrosetti A., Bordas S.P.A., Tkatchenko A. *Phys. Rev. Lett.*, **2022**, *128*, 106101.

[50] Ambrosetti A., Silvestrelli P.L., Tkatchenko A. Physical Adsorption at the Nanoscale: Towards Controllable Scaling of the Substrate-Adsorbate van der Waals Interaction. *Phys. Rev. B*, **2017**, *95*, 235417.

[51] Dobson J. Beyond Pairwise Additivity in London Dispersion Interactions. *Int. J. Quant. Chem.*, **2014**, *114*, 1157-1161.

[52] Tkatchenko A., Ambrosetti A., DiStasio R.A. Interatomic Methods for the Dispersion Energy Derived from the Adiabatic Connection Fluctuation-Dissipation Theorem, *J. Chem. Phys.*, **2013**, *138*, 074106.

[53] Ambrosetti A., Silvestrelli P.L. Hidden by Graphene–Towards Effective Screening of Interface van der Waals Interactions via Monolayer Coating, *Carbon*, **2018**, *139*, 486-491.

[54] Ambrosetti A., Silvestrelli P.L. Faraday-Like Screening by Two-Dimensional Nanomaterials: A Scale-Dependent Tunable Effect. *J. Phys. Chem. Lett.*, **2019**, *10*, 2044-2050.

[55] Dobson J. F., White A., Rubio A. Asymptotics of the Dispersion Interaction: Analytic Benchmarks for van der Waals Energy Functionals *Phys. Rev. Lett.*, **2006**, *96*, 073201.

[56] Dobson J. F. How Many-Body Effects Modify the van der Waals Interaction between Graphene Sheets *Phys. Rev. X*, **2014**, *4*, 021040.

[57] Dobson J. F. Towards Efficient Description of Type-C London Dispersion Forces between Low-Dimensional Metallic Nanostructures. *El. Struc.*, **2021**, *3*, 044001.

[58] Angyan J., Dobson J. F., Jansen G. and Gould T. London Dispersion Forces in Molecules Solids and Nano-Structures: an Introduction to Physical Models and Computational Methods. Chapter 8. *Royal Society of Chemistry*, Cambridge **2020**.

[59] Silvestrelli P.L., Ambrosetti A. Diffusion Quantum Monte Carlo Study of Argon Dimer. *El. Struc.*, **2021**, *3*, 024010.

[60] Medvedev M.G., Bushmarinov I.S., Sun J., Perdew J. and Lyssenko J.P. Density Functional Theory is Straying from the Path toward the Exact Functional. *Science*, **2017**, *355*, 49-52.

[61] J. F. Dobson, B. P. Dinte, and J. Wang, in Electronic Density Functional Theory: Recent Progress and New Directions (Plenum, New York, **1998**), *261*

[62] Oleg A. Vydrov, Troy Van Voorhis. Implementation and assessment of a simple nonlocal van der Waals density functional *J. Chem. Phys.*, **2010**, *132*, 164113.

[63] Bethe H. A., Salpeter E. E. The Quantum Mechanics of one-and two-electron atoms (New York: Plenum) **1977**

[64] A. P. Jones, J. Crain, V. P. Sokhan, T. W. Whitfield, G. J. Martyna, Quantum Drude oscillator model of atoms and molecules: Many-body polarization and dispersion interactions for atomistic simulation *Physical Review B* **2013**, *87*, 144103

[65] Duong, D. L.; Yun, S. J.; Lee, Y. H. van der Waals Layered Materials: Opportunities and Challenges. *ACS Nano* **2017**, *11*, 11803-11830.

[66] Kasai, H.; Tolborg, K.; Sist M.; Zhang, J.; Hathwar, V. R.; Filsø, M. Ø.; Cenedese, S.; Sugimoto, K.; Overgaard J.; Nishibori E. et al. X-ray electron density investigation of chemical bonding in van der Waals materials. *Nature Materials* **2018**, *17*, 249-253.

[67] Medvedev, M. G.; Bushmarinov, I. S.; Sun, J.; Perdew, J. P.; Lyssenko, K. A. Density functional theory is straying from the path toward the exact functional. *Science* **2017**, *355*, 49-52.

[68] Vydrov, O. A.; Van Voorhis, T. Nonlocal van der Waals density functional: The simpler the better. *J. Chem. Phys.* **2010**, *133*, 244103.

[69] Murray, É. D.; Lee, K.; Langreth, D. C. Investigation of Exchange Energy Density Functional Accuracy for Interacting Molecules. *J. Chem. Theory Comput.* **2009**, *5*, 2754-2762.

[70] Jurečka, P.; Šponer, J.; Černý, J.; Hobza, P. Benchmark database of accurate (MP2 and CCSD(T) complete basis set limit) interaction energies of small model complexes, DNA base pairs, and amino acid pairs. *Phys. Chem. Chem. Phys.* **2006**, *8*, 1985-1993.

[71] Perdew, J. P.; Wang, Y. Accurate and simple analytic representation of the electron-gas correlation energy. *Phys. Rev. B* **1992**, *45*,

[72] Román-Pérez, G.; Soler, J. M. Efficient Implementation of a van der Waals Density Functional: Application to Double-Wall Carbon Nanotubes. *Phys. Rev. Lett.* **2009**, *103*, 096102.

[73] Giannozzi, P.; Baroni, S.; Bonini, N.; Calandra, M.; Car, R.; Cavazzoni, C.; Ceresoli, D.; Chiarotti, G. L.; Cococcioni, M.; Dabo, I. QUANTUM ESPRESSO: a modular and open-source software project for quantum simulations of materials. *Journal of Physics: Condensed Matter* **2009**, *21*, 395502-395521.

[74] Giannozzi, P.; Andreussi, O.; Brumme, T.; Bunau, O.; Buongiorno Nardelli, M.; Calandra, M.; Car, R.; Cavazzoni, C.; Ceresoli, D.; Cococcioni, M. et al. Advanced

capabilities for materials modelling with Quantum ESPRESSO. *Journal of Physics: Condensed Matter* **2017**, *29*, 465901-465931 .

[75] http://www.quantum-espresso.org/pseudopotentials

[76] Blöchl, P. E. Projector augmented-wave method. *Phys. Rev. B* **1994**, *50*, 17953-17979.

[77] Charles, H. A.; Meyer, W. W. Optimal Error Bounds for Cubic Spline Interpolation. *Journal of Approximation Theory* **1976**, *16*, 105-122.

[78] Otero-de-la-Roza A.; Blanco, M. A.; Pendás, A. M.; Luaña, V. Critic: a new program for the topological analysis of solid-state electron densities. *Comput. Phys. Commun.* **2009**, *180*, 157-166.

[79] Otero-de-la-Roza, A.; Johnson, E. R.; Luaña, V. Critic2: a program for real-space analysis of quantum chemical interactions in solids. *Comput. Phys. Commun.* **2014**, *185*, 1007-1018 .

[80] Yourdshahyan, Y.; Zhang, H. K.; Rappe, A. M. n-alkyl thiol head-group interactions with the Au(111) surface. *Phys. Rev. B* **2001**, *63*, 081405.

[81] Peng, H.; Yang, Z. H.; Perdew, J. P.; Sun, J. Versatile van der Waals Density Functional Based on a Meta-Generalized Gradient Approximation. *Phys. Rev. X* **2016**, *6*, 041005.

[82] Björkman, T.; Gulans, A.; Krasheninnikov, A. V.; Nieminen, R. M. van der Waals Bonding in Layered Compounds from Advanced Density-Functional First-Principles Calculations. *Phys. Rev Lett.* **2012**, *108*, 235502.

[83] Clerc, D. G.; Poshusta, R. D.; Hess, A. C. Periodic Hartree-Fock Study of TiS_2. *J. Phys. Chem.* **1996**, *100*, 15735-15747.

[84] Troullier, N.; Martins, J. L. Efficient pseudopotentials for plane-wave calculations. *Phys. Rev. B* **1991**, *43*, 1993-2006.

[85] Louie, S. G.; Froyen, S.; Cohen, M. L. Nonlinear ionic pseudopotentials in spin-density-functional calculations. *Phys. Rev. B* **1982**, *26*, 1738-1742.

[86] Qin, Z.; Wang, L.; Cong, R.; Jiao, C.; Zheng, X.; Cui, Z.;Tang, Z. Spectroscopic identification of the low-lying states of S_2 molecule. *J. Chem. Phys.* **2019**, *150*, 0443025.